Effect of thermal nonequilibrium on the shock interaction mechanism for carbon dioxide mixtures on double-wedge geometries

View Online   Export Citation   CrossMark

Catarina Garbacz,[a] (iD) Fábio Morgado, (iD) and Marco Fossati (iD)

AFFILIATIONS

Aerospace Centre, University of Strathclyde, Glasgow G1 1XQ, United Kingdom

[a]Author to whom correspondence should be addressed: ana.gomes@strath.ac.uk

ABSTRACT

The effect of thermal nonequilibrium on shock interactions of carbon dioxide (CO_2) hypersonic flows is investigated. Given the relatively low characteristic vibrational temperature of the CO_2 molecule, it is expected that excited vibrational modes play a significant role in the physics of shock/shock and shock/boundary layer interactions. The shock interference mechanism resulting from a CO_2-dominated flow over different double-wedge geometries is investigated by numerically solving the Navier–Stokes equations within the framework of a two-temperature model that considers translational energy–vibrational energy transfer. To assess the impact of vibrational relaxation, a comparative assessment of the patterns obtained with three thermo-physical models is presented, with the two-temperature model flow pattern being compared to thermally perfect and perfect ideal gas ones. Results obtained with the two-temperature model show that increasing the aft angle significantly enlarges the separated region in the compression corner and generates numerous secondary shock waves and shear layers. Peaks of heat flux and pressure occur along the surface due to boundary layer reattachment downstream of the compression corner, except for the case of the higher angle, which results in the largest peaks due to shock impingement. Different assumptions on the excitation of vibrational modes are shown to largely influence the size of the recirculation bubble in the compression corner, shock interaction mechanism, and surface loads. The more energy transferred to the vibrational mode, the lower post-shock temperatures are obtained, which tends to reduce the post-shock density, leading to weaker shock interactions characterized by delayed onsets of separation, reduced separation regions, and smaller standoff distances.

I. INTRODUCTION

Predicting shock–shock and shock–boundary layer interactions (SBLIs) is a fundamental problem of fluid mechanics and has important consequences in the design of high-speed vehicles. Interference of shock waves and boundary layers can be observed near compression corners such as the ones found near control surfaces, wing–fuselage junction, or inlet of propulsive systems. One of the main issues associated with this interaction is the occurrence of localized fairly high heating and pressure loads along the surface of the vehicle resulting from the shock waves' interaction and their influence on the development of the boundary layer. The location and strength of these surface loads may change in time in cases where the nature of the flow is unsteady, and accurately estimating such mechanisms of shock interaction is crucial to prevent catastrophic failures such as the case of the NASA X-15.[1] When the internal energy of the flow is increased across a shock wave, a process of energy transfer is established between the internal degrees of freedom of the molecules (translational, rotational, vibrational, and electronic). When the number of molecular interactions occurring during the characteristic flow time is small, the mechanism of energy transfer is often found to be in a nonequilibrium state. Nonequilibrium energy transfer mechanisms substantially influence the intensity of the different waves and flow mechanisms taking place in the interaction region.

The phenomenon of shock wave interference has been extensively investigated in the case of air, with application to re-entry and transatmospheric hypersonic flight in Earth's atmosphere. The first studies were carried out by Edney,[2] who investigated experimentally the impingement of an oblique shock over a bow shock (BS) in front of a cylinder. Depending on the angle of the oblique shock and, consequently, the location of the intersection, distinct wave patterns were

identified and classified into six different shock interaction types using a shock-polar approach. This pioneering classification has since been used in subsequent works, not only in the case of a cylinder oblique/ bow shock interaction, but also in the case of the flow over double-wedge and double-cone configurations. These idealized cases of hypersonic flow over the compression corner have been widely studied in the literature due to their geometric simplicity and because they are often encountered in actual vehicle design.[3,4] Inviscid air flow over double-wedges under the perfect gas assumption ($\gamma = 1.4$) was numerically studied by Olejniczak et al.[5] in order to identify the shock interaction patterns resulting from a fixed fore wedge angle of 15° and increasing angle of the second wedge from 35° to 60° in increments of 5°. The study revealed a transition from type VI → V → IV and new interaction type IVr for the higher aft wedge angle.

Extensive efforts have also been made in the attempt to better understand the physics of shock interactions in the presence of viscous effects. In 2015, Tumuklu et al. investigated viscous laminar shock interactions in a Mach 7 flow over a 30°–55° double-wedge configuration using DSMC (Direct Simulation Monte Carlo).[6] They compared the behavior of the flow for three different gas mixtures: air, nitrogen, and argon. A comparison with experimental data revealed that the numerical model based on a macroscopic approach has succeeded in providing insight into the physics of complex nonequilibrium flows, as a good agreement for both the unsteady shock wave system and surface heat flux distribution was obtained. Moreover, the size of the separation region, the upstream movement of the triple-point, and the time for the flow to reach steady state revealed to be much less for air than for the case of nitrogen. The flow of argon exhibited the fastest movement of the triple-point relative to the other two mixtures. In 2016, the role of gas mixtures on the shock interaction mechanism was further investigated.[7] It was concluded that the relative magnitude of the specific heat ratio has a significant impact on SBLIs (shock–boundary layer interactions). More specifically, the flow of argon resulted in a separation bubble with 1.8 times the size of the one for nitrogen and—due to the endothermic effects of finite-rate chemistry—the size of this region was 1.5 smaller for air than for nitrogen.

Previous findings expose the sensitivity of flow patterns to the thermodynamic properties of the mixture. Youssefi and Knight[8] conducted a numerical study to assess the CFD (computational fluid dynamics) capabilities in predicting shock wave–laminar boundary layer interaction for the double-cone configuration when different assumptions for thermodynamics and chemical-kinetics are employed. Four separate cases were simulated for air with stagnation enthalpies ranging from 5.44 to 21.77 MJ/kg and Mach numbers from 10.9 to 12.82 and the results were compared against experimental data. A comparison between the equilibrium perfect gas model and a thermodynamic/thermochemical nonequilibrium model (NEQ) (considering one equation for mass and one equation for vibrational energy conservation per chemical species) revealed that the latter model underpredicts the size of the separation region for all cases except 21.77 MJ/kg, but that the pressure plateau in this region, as well as the location of peak pressure and heat flux at reattachment, agrees well with the experiment. To better understand the discrepancies of previous studies when it comes to accurately predicting the size of the separation region, Hao and Wen[9] investigated the effects of modeling vibrational nonequilibrium in air flows using different assumptions: (1) a mixture of perfect gases with vibrational nonequilibrium of the mixture, (2) a

mixture of perfect gases with vibrational nonequilibrium of separate modes, and (3) a mixture of calorically perfect gases. Results showed that, in comparison with model 1, considering separate vibrational modes slightly increases the size of the separation bubble, whereas excluding vibrational excitation significantly enlarges it. It was seen that considering vibrational excitation generally results in a detached shock that is closer to the surface, which was attributed to the fact that this process absorbs the translational energy of the flow, which reduces the post-shock temperatures and increases density, leading to a smaller shock standoff distance. Khraibut and Gai further investigated the impact of real gas effect in shock interactions.[10] It was shown that real gas effects stabilize the entire flow and have a significant impact on the size of the separation bubble, whereas no impact is seen in the flow prior to separation. The study also revealed that, contrary to what was obtained with earlier perfect gas simulations, a steady state is reached when real gas effects are taken into account.

Several research studies have focused on understanding sources of unsteadiness and coupling between the various flow features. Durna et al. have numerically analyzed a 2.1 MJ/kg low-enthalpy Mach 7 flow of nitrogen over four different double-wedge configurations,[11] with a fore angle of 30° and the aft angle systematically increased from 45° to 60°. Increasing the aft angle resulted in significant differences in the flow physics. A strong coupling between the deformation of the boundary layer and the bow shock as well as transmitted shock (TS) was observed for the higher aft angles. It was found that there is a threshold value of the aft angle, between 45° and 50°, below which the flow reaches steady state and above which becomes periodic in time. Further work was carried out to investigate the periodicity of interactions for the higher aft angles of 50°, 55°, and 60°.[3] By analyzing density gradients, shock locations, separation angle, and the distributions of pressure and heat flux along the surface of the wedges, it was concluded that when the aft angle is increased, the period of flow shortens, the duration of impingement of the transmitted shock on the wedge surface decreases, the number of vortexes near the compression corner increases, the distance from the leading edge to the separation point shortens, and the separation region becomes longer and thicker. Very recently, Kumar and De investigated the origin and sustenance of oscillatory shock structures in a nitrogen flow over a 30°–55° double-wedge.[12] The size of the separation bubble is shown to influence the overall shock interaction pattern, also determining whether the flow is steady or not. The presence of an incident shock just downstream of the expansion corner while the separation region is overstretched shows to be the parameter dictating the steady or periodic nature of the flow. It is concluded that different shock interaction patterns can be obtained by varying different geometrical parameters; however, it is only when the incidence shock crosses the expansion corner, disturbing the process of relaxation of the separation region, that the flow repeats its previous cycle and becomes periodic. Extending the work presented in Ref. 11, Vatansever and Celik mirrored the numerical study for the case of high-enthalpy flows with a stagnation enthalpy of 8.0 MJ/kg.[13] It was seen that, as the aft angle is increased, the magnitudes of wall heat flux and surface pressure are enhanced, especially in the vicinity of the separation zone, as a result of stronger shock interactions. Additionally, it was observed that fluctuation magnitudes and time-averaged values of the surface loads were significantly larger on the surface of the second wedge.

Despite the number of studies carried out to expand the knowledge on the physics of shock interactions for air, mixtures of molecular

nitrogen (N_2) or molecular oxygen (O_2), little work has been done for other gas mixtures. With recent space programs for missions to Mars, the research community has raised interest in its atmosphere, which is mainly composed of carbon dioxide (CO_2).[14–20] As stated by Tumuklu *et al.*, the thermodynamic characteristics of a mixture play an important role in the behavior of shock interactions.[6] The CO_2 chemical species is a triatomic molecule whose structure differs from the diatomic ones encountered in air (N_2, O_2) in terms of the behavior of the vibrational degrees of freedom and subsequent energy redistribution among the various internal modes. This results in a characteristic vibrational temperature that is lower than in the case of air, with a non-negligible impact on the nonequilibrium processes. Candler[14] simulated a Martian atmospheric entry flow of CO_2–N_2 and has shown that, due to the very fast vibrational relaxation of CO_2, there was only a small region of the flow exhibiting thermal nonequilibrium. The two-temperature nonequilibrium model for CO_2 was later developed by Park.[15] By applying the model to a re-entry simulation of a stagnation-line flow, the conclusions drawn by Candler were confirmed. Windisch *et al.*[16] simulated the impingement of an oblique shock on a bow shock in front of a cylinder in a CO_2-dominated flow, and a type VII interaction pattern was obtained. A comparison with the same test case, but considering instead an N_2 mixture, revealed that the post-shock temperatures were significantly lower for the gas model of the Martian atmosphere, resulting in a higher fluid density and a much smaller shock standoff distance. Moreover, regions of thermal non-equilibrium were very small, due to fast vibrational relaxation. Recent studies conducted by the authors of the present paper compared shock interaction patterns resulting from an inviscid Mach 9 flow over a double-wedge, for air and CO_2–N_2 mixtures.[21] Numerical results have shown that, for lower freestream temperatures, the nonequilibrium shock interaction patterns differ between air and CO_2 flow, with a large impact on the surface pressure distribution. A comparison with a perfect ideal gas (PIG) model revealed that, despite the small degree of thermal nonequilibrium encountered in the case of CO_2 relative to the flow of air, it still has a significant impact on the obtained interaction pattern.

The objective of this study is to extend the understanding of nonequilibrium shock interaction physics in CO_2-dominated flows by means of numerical modeling and simulation at the hydrodynamic scale. A number of experimental studies have been carried out to better understand the physics of hypersonic air or nitrogen flows over double-wedges.[22,23] However, most experimental studies concerning flows of CO_2 refer to blunt bodies,[24–30] for which the physics is essentially very different from that occurring over double-wedges. Numerical tools remain the most affordable and accessible approach to tackle the problem of CO_2 flows over double-wedges. Detailed models that consider the separation of different vibrational modes of CO_2 have been derived on the basis of the kinetic theory.[18–20] Nevertheless, it has been shown that for CFD applications with flow conditions for which deviations from equilibrium are not extreme, a two-temperature model can be adequate and offer a good compromise between accuracy and computational cost. We conduct a systematic numerical study of a laminar viscous Mach 9 CO_2–N_2 flow over a double-wedge geometry with a fore angle of $15°$ and an aft angle increasing from $40°$ to $55°$ in increments of $5°$. Results are obtained with the widely used two-temperature model by Park,[15] which assumes that the vibrational modes may relax considerably slower

than the rate of fluid motion, therefore considering a separate vibrational temperature of the mixture. To better understand the role of vibrational excitation and internal energy transfer on the patterns of interaction and surface loads, the nonequilibrium solutions are compared to the thermally perfect gas (TPG) model—which implicitly accounts for vibrational excitation by having thermodynamic properties such as specific heats changing accordingly with temperature and considering one temperature only—and the more simplified perfect ideal gas model, which does not account for the excitation of internal degrees of freedom (rotational, vibrational, and electronic). Simulations are performed with the open-source CFD code SU2[31] coupled to the thermochemistry Mutation++ library.[32]

This paper is organized as follows: Section II introduces the governing equations and physical models. Section III gives an overview of the numerical modeling, including details on the solvers, computational domain, boundary conditions, and grid convergence study. Section V presents the nonequilibrium shock interaction mechanisms obtained in this study. Section VI shows the impact of different thermo-physical models on the separation and wave structures and eventually, in Sec. VII, the main conclusions are presented.

II. PHYSICAL MODELING

The system of governing equations implemented with the nonequilibrium models follows the Navier–Stokes approach presented in the literature for a continuum, viscous laminar, thermal nonequilibrium flow with finite-rate chemistry.[33] The two-temperature model by Park is used to model thermal nonequilibrium. It has been developed initially for air[34] but later modified for CO_2 flows[15] and validated in Refs. 30 and 35 against experimental data and the more detailed state-to-state approach. The model assumes that rotational relaxation is very fast relative to the rate of fluid motion and therefore considers that the translational and rotational modes of the gas are in equilibrium with each other at the translational-rotational temperature T_{tr}. As for vibrational relaxation, the CO_2 triatomic molecule has three vibrational modes, one of which is double degenerate. Camac[36] showed that all three modes relax at the same time, but considerably slower than the rate of fluid motion, leading to a single separate temperature to describe this process. Electronic modes are assumed to be at equilibrium with vibration, therefore it is considered that these two modes relax at the vibro-electronic temperature T_{ve}. In a compact form, the system of equations can be described as follows:

$$\frac{d\mathbf{U}}{dt} + \nabla \cdot \vec{\mathbf{F}}^c(\mathbf{U}) = \nabla \cdot \vec{\mathbf{F}}^v(\mathbf{U}) + \mathbf{Q}(\mathbf{U}), \quad (1)$$

where the conservative variables, convective fluxes, viscous fluxes, and source terms are given by

$$\mathbf{U} = \begin{Bmatrix} \rho_1 \\ \cdots \\ \rho_{n_s} \\ \rho\vec{u} \\ \rho e \\ \rho e^{ve} \end{Bmatrix}, \quad \vec{\mathbf{F}}^c = \begin{Bmatrix} \rho_1\vec{u} \\ \cdots \\ \rho_{n_s}\vec{u} \\ \rho\vec{u} \otimes \vec{u} + p\bar{I} \\ \rho h\vec{u} \\ \rho e^{ve}\vec{u} \end{Bmatrix}, \quad (2)$$

$$\mathbf{F}^{\mathrm{v}} = \begin{Bmatrix} \vec{J}_1 \\ \cdots \\ \vec{J}_{n_s} \\ \bar{\tau} \\ \bar{\tau} \cdot \vec{u} + \sum_s \vec{J}_s h_s + \vec{q}^{\,\mathrm{ve}} + \vec{q}^{\,\mathrm{tr}} \\ \sum_s \vec{J}_s h_s^{\mathrm{ve}} + \vec{q}^{\,\mathrm{ve}} \end{Bmatrix}, \quad \mathbf{Q} = \begin{Bmatrix} \dot{\omega}_1 \\ \cdots \\ \dot{\omega}_{n_s} \\ 0 \\ 0 \\ \dot{\Omega} \end{Bmatrix}, \quad (3)$$

and ρ is the density of the mixture; ρ_s is the partial density of species s; p is the static pressure; e and e^{ve} are, respectively, the total energy per unit mass and the vibrational energy per unit mass for the mixture; h is the total enthalpy per unit mass; $\vec{J}_s$ is the species mass diffusion flux; $\bar{\tau}$ is the viscous stress tensor; $\vec{q}$ is the conduction heat flux; index s denotes the sth chemical species; and n_s is the total number of species.

Calculating the nonequilibrium thermodynamic state and source terms is necessary to close the system of governing equations that describes hypersonic flows. This is achieved by means of coupling with appropriate multi-temperature thermochemistry models. The equations presented below describe the implementation of the two-temperature model for a mixture composed of neutral species, provided by the Mutation++ library.[32] Each individual species s is assumed to behave as an ideal gas. Hence, the total pressure of the mixture p is defined by Dalton's law as the summation of the partial pressures associated with each species p_s, determined by the ideal gas law

$$p = \sum_{s=1}^{n_s} p_s = \sum_{s=1}^{n_s} \rho_s \frac{R_{\mathrm{u}}}{M_s} T_{\mathrm{tr}}, \quad (4)$$

where R_{u} is the universal gas constant, M_s is the molar mass of species s, and T_{tr} is the trans-rotational temperature. The total specific energy of the flow e is given as the sum of the internal and kinetic energies, i.e.,

$$e = \sum_{s=1}^{n_s} c_s e_s + \frac{1}{2} u^2, \quad (5)$$

where c_s is the mass fraction of species s, u is the magnitude of the flow velocity vector, and e_s is the specific internal energy of the species, given by the sum of the energy of formation and the contribution of each internal mode (t—translational, r—rotational, v—vibrational, e—electronic), i.e.,

$$e_s = e_s^{\mathrm{t}}(T_{\mathrm{tr}}) + e_s^{\mathrm{r}}(T_{\mathrm{tr}}) + e_s^{\mathrm{v}}(T_{\mathrm{ve}}) + e_s^{\mathrm{e}}(T_{\mathrm{ve}}) + e_s^0. \quad (6)$$

Using a combination of statistical thermodynamics and quantum mechanics, the internal mode energies are defined on the basis of the Rigid-Rotor Harmonic Oscillator model as follows:

$$e_s^{\mathrm{t}}(T_{\mathrm{tr}}) = \frac{3}{2} \frac{R_{\mathrm{u}}}{M_s} T_{\mathrm{tr}}, \quad (7)$$

$$e_s^{\mathrm{r}}(T_{\mathrm{tr}}) = \begin{cases} \dfrac{R_{\mathrm{u}}}{M_s} T_{\mathrm{tr}}, & \text{for linear molecules,} \\ 0, & \text{for atoms,} \end{cases} \quad (8)$$

$$e_s^{\mathrm{v}}(T_{\mathrm{ve}}) = \begin{cases} \dfrac{R_{\mathrm{u}}}{M_s} \sum_v \dfrac{\theta_{v,s}^{\mathrm{v}}}{\exp(\theta_{v,s}^{\mathrm{v}}/T_{\mathrm{ve}}) - 1}, & \text{for molecules,} \\ 0, & \text{for atoms,} \end{cases} \quad (9)$$

$$e_s^{\mathrm{e}}(T_{\mathrm{ve}}) = \frac{R_{\mathrm{u}}}{M_s} \frac{\sum_i g_{i,s} \theta_{i,s}^{\mathrm{e}} \exp(-\theta_{i,s}^{\mathrm{e}}/T_{\mathrm{ve}})}{\sum_i g_{i,s} \exp(-\theta_{i,s}^{\mathrm{e}}/T_{\mathrm{ve}})}, \quad (10)$$

where $\theta_{v,s}^{\mathrm{v}}$ is the characteristic vibrational temperature of species s and vibrational mode v and $g_{i,s}$ and $\theta_{i,s}^{\mathrm{e}}$ are the degeneracy and characteristic electronic temperature, respectively, at energy level i for species s. The formation energy e_s^0 is referenced at the standard state conditions of 298.15 K and 1 atm.

The conservation equation for the mass of the mixture is replaced by a mass conservation equation for each species in the gas, incorporating a production/destruction term that results from chemical activity. The chemical source term $\dot{\omega}_s$ is given by

$$\dot{\omega}_s = M_s \sum_{r=1}^{n_r} (\nu_{s,r}'' - \nu_{s,r}') \left[k_{\mathrm{f},r} \prod_{j=1}^{n_s} \hat{\rho}_j^{\nu_{j,r}'} - k_{\mathrm{b},r} \prod_{j=1}^{n_s} \hat{\rho}_j^{\nu_{j,r}''} \right], \quad (11)$$

where n_r and n_s are, respectively, the number of reactions and the number of species; ν_s' is the forward reaction stoichiometry coefficient; ν_s'' is the backward reaction stoichiometry coefficient; $\hat{\rho}_j$ is the molar density; $k_{\mathrm{f},r}$ is the forward reaction rate; and $k_{\mathrm{b},r}$ is the backward reaction rate. The forward reaction rate for each reaction r is defined according to the modified Arrhenius equation given by

$$k_{\mathrm{f},r} = A_r T_{\mathrm{c}}^{N_r} \exp\left(-\frac{\theta_r}{T_{\mathrm{c}}}\right), \quad (12)$$

where the coefficients A_r, θ_r, and N_r are obtained from experimental data and are, respectively, the reaction rate constant, the activation temperature, and an exponent. The backward reaction rates $k_{\mathrm{b},r}$ are determined from the equilibrium reaction rates, $k_{\mathrm{b},r} = k_{\mathrm{f},r}/k_{\mathrm{eq},r}$ for every reaction r. The equilibrium reaction rates $k_{\mathrm{eq},r}$ are determined as a function of the Gibbs free energy. T_{c} is the controlling temperature determined by Park's two-temperature model as follows:[37]

- For dissociation reactions $\mathrm{AB} + \mathrm{M} \rightleftharpoons \mathrm{A} + \mathrm{B} + \mathrm{M}$, $T_{\mathrm{c}} = \sqrt{T_{\mathrm{tr}} T_{\mathrm{ve}}}$ for the forward rate; $T_{\mathrm{c}} = T_{\mathrm{tr}}$ for the backward rate.
- For exchange reactions $\mathrm{AB} + \mathrm{C} \rightleftharpoons \mathrm{A} + \mathrm{BC}$, $T_{\mathrm{c}} = T_{\mathrm{tr}}$.

In the two-temperature model, the energy transfer mechanisms, which determine the change in vibrational energy of the mixture, are accounted for in the source term vector. The source term $\dot{\Omega}$ is defined as the sum of the vibrational-to-translational energy transfer and energy exchanges due to chemical activity as follows:

$$\dot{\Omega} = \sum_{s=1}^{n_s} \dot{\Omega}_s^{\mathrm{tr:ve}} + \dot{\Omega}_s^{\mathrm{c:v}} + \dot{\Omega}_s^{\mathrm{c:e}}. \quad (13)$$

The term $\dot{\Omega}^{\mathrm{tr:ve}}$ concerns the rate of energy exchange between the translational and vibrational energy modes, following the Landau–Teller model,[38]

$$\dot{\Omega}_s^{\mathrm{tr:ve}} = \rho_s \frac{e_s^{\mathrm{v}}(T) - e_s^{\mathrm{v}}(T_{\mathrm{v}})}{\tau_s^{\mathrm{V-T}}}. \quad (14)$$

The vibrational relaxation time of each species, $\tau_s^{\mathrm{V-T}}$, is given by the Millikan and White empirical formula[39] and the Park correction as follows:[37]

$$\tau_s^{\text{V-T}} = \tau_s^{\text{MW}} + \tau_s^{\text{P}}, \tag{15}$$

where the Millikan and White relaxation time of species s depends on the vibrational relaxation times of the interactions with collision partners r and the corresponding molar fractions X_r, as follows:

$$\tau_s^{\text{MW}} = \left(\sum_{r=1}^{n_s} \frac{X_r}{\tau_{s-r}^{\text{MW}}} \right)^{-1}, \tag{16}$$

$$\tau_{s-r}^{\text{MW}} = \exp\left(A_{s,r} \left(T^{-\frac{1}{3}} - B_{s,r} \right) - 18.42 \right) \left(\frac{p}{101325} \right)^{-1} [\text{s}]. \tag{17}$$

The Park correction is given by

$$\tau_s^{\text{P}} = \left(N_s \sigma_s \sqrt{\frac{8 R_u T_{\text{tr}}}{\pi M_s}} \right)^{-1}, \tag{18}$$

where r denotes the rth species, X_r is the molar fraction, N_s is the number density, and σ_s is an effective cross section for vibrational relaxation. The change in vibrational-electronic energy of the mixture due to the production/destruction of species is accounted for in the terms $\dot{\Omega}_s^{\text{c:v}}$ and $\dot{\Omega}_s^{\text{c:e}}$, given by

$$\dot{\Omega}_s^{\text{c:v}} = c_1 \dot{\omega}_s e_s^{\text{v}}, \qquad \dot{\Omega}_s^{\text{c:e}} = \dot{\omega}_s e_s^{\text{e}}. \tag{19}$$

A non-preferential dissociation model is considered to account for the coupling between vibrational energy modes and finite-rate chemistry. The model assumes that molecules are destroyed or created at the average vibrational energy of the cell, $c_1 = 1$.

With regard to dissipative fluxes, the mass diffusion flux of each species $\vec{J}_s$ is described by Fick's law of diffusion, i.e.,

$$\vec{J}_s = \rho_s \vec{V}_s, \tag{20}$$

where $\vec{V}_s$ is the element diffusion velocity, obtained by solving the Stefan–Maxwell equations under the Ramshaw approximation. The viscous stress tensor is written in vector notation as

$$\bar{\tau} = \mu \left(\nabla \vec{u} + \nabla \vec{u}^{\text{T}} - \frac{2}{3} \bar{I} (\nabla \cdot \vec{u}) \right), \tag{21}$$

where μ is the mixture viscosity coefficient. The conduction heat flux for each thermal energy mode $\vec{q}_k$ is assumed to be given by Fourier's law of heat conduction, i.e.,

$$\vec{q}_k = \lambda_k \vec{\nabla}(T_k), \tag{22}$$

where T_k is the temperature and λ_k is the thermal conductivity coefficient of the kth energy mode. Viscosity μ and mode thermal conductivity λ_k are computed using Wilke's mixing rule.[40] The species thermal conductivity is calculated using Eucken's formula[41] that takes into account both translational and vibrational temperatures.

III. NUMERICAL MODELING

The governing equations introduced in Sec. II are numerically solved with an open-source CFD code that has been extensively validated.[31,42,43] The software is built for multiphysics analysis and design, including a framework of both equilibrium and nonequilibrium models. The closure of the governing equations for the system of interest is achieved by means of coupling with appropriate thermochemistry

models. In this regard, the CFD solver is linked to an external library that provides efficient algorithms for the computation of thermodynamic, transport (viscosity, thermal conductivity, and diffusion), and chemical kinetic gas properties for a given state of the mixture. The library has been designed for robustness over a wide range of temperatures and its accuracy in dealing with multi-temperature models. The library has been extensively validated as a software on its own[32] and some validation work has been carried out for the coupling with the CFD solver.[44] The approach adopted for numerical discretization is a finite-volume edge-based formulation used with the AUSM scheme[45] (Advection Upstream Splitting Method) together with MUSCL (Monotonic Upstream-centered Scheme for Conservation Laws) and the Venkatakrishnan–Wang limiter. A dual time-stepping approach with a second-order backward-difference discretization is adopted to address unsteadiness.

A. Domain, boundary conditions, and simulation parameters

The double-wedge geometry considered in this study is illustrated in Fig. 1. Four different configurations are considered with a fixed fore angle of $15°$ and aft angles of $40°$, $45°$, $50°$, and $55°$. For all cases, $L_1 = L_2 = 0.2$ m. The two wedge surfaces and the expansion surface downstream of the expansion corner are assumed to be isothermal walls. For the leftmost horizontal segment, a symmetry boundary condition is applied. An outlet boundary condition is chosen for the exit and farfield is considered for the remaining boundaries. Numerical simulations are performed for a flow of CO_2:97%, N_2:3% referring to the atmosphere of Mars. Simulation parameters, presented in Table I, are chosen so that the freestream conditions are in the laminar continuum regime and values of pressure and temperature that can be found in the Martian atmosphere. The freestream flow is assumed to be in thermal equilibrium.

B. Grid independence

As previously discussed, the flow physics encountered in this type of flow is rather complex, including features such as shock waves, boundary layer, and contact discontinuities (CSs). These features are
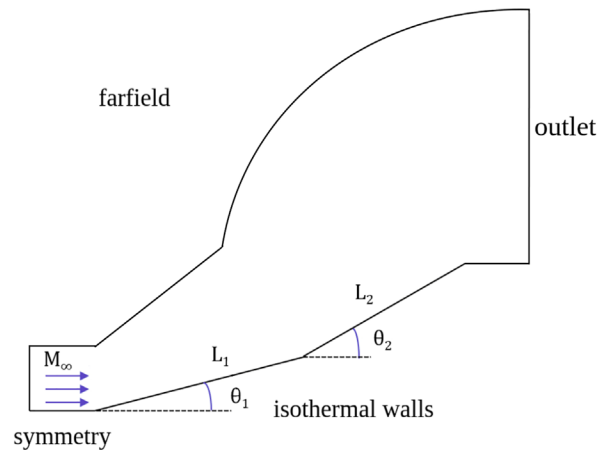

FIG. 1. Double-wedge geometry and boundary conditions.

TABLE I. Simulation parameters.

M_∞	p_∞ (Pa)	T_∞ (K)	T_{wall} (K)	Mole fractions
9	10	160	300	CO_2:0.97 N_2:0.03

very localized, highly directional, and characterized by sharp gradients. Moreover, they usually separate regions of nearly uniform flow. To guarantee minimum computational waste in accurately capturing shock interaction mechanisms, automatic anisotropic mesh adaptation is used to generate meshes. Anisotropic meshes allow for a clustering of nodes and stretching of the elements in such a way that the element faces are well-aligned with the flow features and no significant increase in number of nodes is necessary to improve the accuracy of the solution.

The mesh adaptation library is a fast, robust, and automatic tool that performs anisotropic mesh adaptation for complex geometries generating multi-scale and multi-direction phenomena in the flowfield (shock waves, contact discontinuities, boundary layers, turbulence, etc.).[46–49] Given an initial mesh and associated CFD solution, a metric field is computed from interpolation error and surface geometric approximation. The metric field provides information about the desired element sizes and orientations in order to drive adaptation. For a finite volume solution, the interpolation error of any particular flow variable is second-order in space. The software performs successive local mesh modifications such as edge collapse, point insertion, edge swapping, and point smoothing until the output mesh meets the metric requirements, as well as some mesh quality constraints to ensure the stability and enhance the performance of the CFD solver. The solution is then interpolated onto the new mesh. More information about the process as well as detailed mathematical formulation can be found in Ref. 49.

The Mach number is chosen as a variable to compute the metric field used for adaptation since all the flow features translate to Mach number gradient and are therefore recognized by the adaptation process. Grid convergence is assessed qualitatively, on the basis of the establishment of a given shock interaction pattern, and quantitatively, by comparing the normalized wall surface pressure, the wall surface heat flux, and the normalized temperature profile normal to the wall at two given locations where relevant flow features are present. A grid convergence study was performed for all test cases, but for simplicity, only the case of the 15°–50° double-wedge with the thermally perfect gas model is showcased here. A representation of the original hybrid mesh used for all test cases is shown at the top of Fig. 2 and the final adapted mesh for the case of the 15°–50° double-wedge with the thermally perfect gas model is shown at the bottom. The two red lines 1 and 2 indicate the positions along the surface of each wedge where the temperature profile normal to the wall is evaluated. Quantitative comparisons for the different levels of adaptation are shown in Fig. 3. Results obtained for levels 2 and 3 are almost identical, proving grid convergence.

IV. VISCOUS FLOW PHYSICS OVER DOUBLE-WEDGES

Recent results on shock wave interaction patterns in CO_2 flows over a double-wedge addressed inviscid flows.[44] When viscous effects are present, shock waves and slip lines are no longer discontinuities, but take the form of high-gradient regions, which may have an
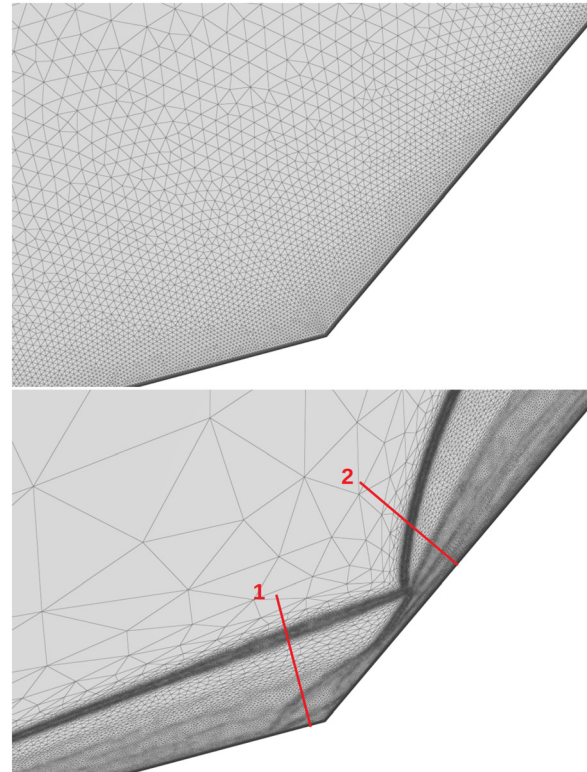

FIG. 2. Original and final hybrid adapted grid for the 15°–50° TPG test-case. Close-up near the compression corner.

substantial impact on how the flow develops and in turn may exhibit interesting nonequilibrium effects. The presence of a possibly non-equilibrium thermal boundary layer generates a gradient of temperature near the wall that influences the surface aerodynamic heating. Furthermore, the inclusion of viscous effects in the simulation of this type of flows generates additional flow features such as boundary layers, recirculation zones, and vortices. The interaction between different shock waves and the flow features arising from viscous effects leads to increasingly complex flow physics that can result in localized severe peaks of pressure and heat flux along the surface.

The leading shock (LS) generated at the beginning of the first wedge intersects the separation shock caused by the recirculation bubble occurring in the compression corner. While Fig. 4 sketches conceptually the key features expected to occur near the compression corner when a viscous flow is considered, the actual and detailed flow pattern depends on the geometry of the ramps, the freestream conditions, and the thermochemical characteristics of gas. As the boundary layer develops along the surface of the fore wedge, it is affected by the adverse pressure gradient resulting from the presence of the second wedge. The adverse pressure gradient potentially leads to boundary layer separation and the separation point gradually moves upstream. The boundary layer then reattaches at a certain location on the aft wedge surface and a recirculation bubble is formed below the slip line. This bubble acts as a new wedge, since the supersonic flow over the slip line is forced to adopt the new velocity direction. In addition to
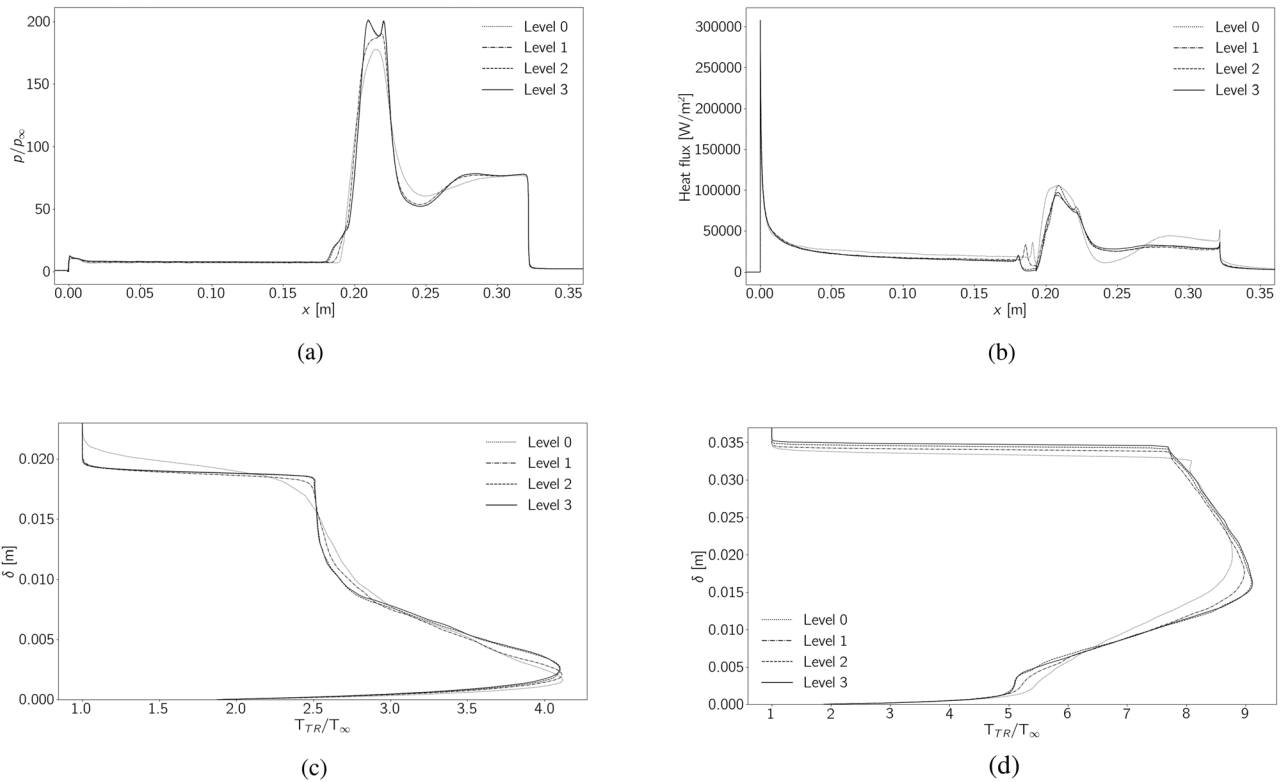
FIG. 3. Grid convergence study for the case of the 15°–50° double-wedge with thermally perfect gas model: (a) normalized surface pressure, (b) surface heat flux, (c) normalized temperature in location 1, and (d) normalized temperature in location 2.

the presence of a separation/detachment shock (DS) wave, reattachment of the boundary layer leads to a series of compression waves (CWs) that may coalesce and form another shock. At the reattachment point, the boundary layer becomes very thin and the pressure is high, resulting in a region of very high aerodynamic heating.[50] Moreover, the shock wave interaction over the double-wedge may result in impingement on the surface, as illustrated in Fig. 5. Given the presence of viscous effects, the impinging shock interacts with the boundary layer (SBLI), introducing an adverse gradient of pressure. If this interaction is strong enough, it causes the boundary layer to separate in the vicinity of the impingement point, generating additional separation and reattachment shocks (ReS). Depending on the considered free-stream conditions, gas mixture, and angles of each wedge, the flow physics resulting from the interference of various features will result in different shock interaction mechanisms.[51] Section V will discuss the different mechanisms of interaction obtained for the geometry illustrated in Fig. 1 and flow conditions shown in Table I.
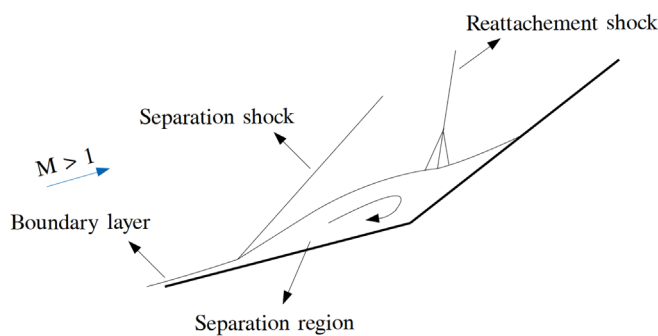
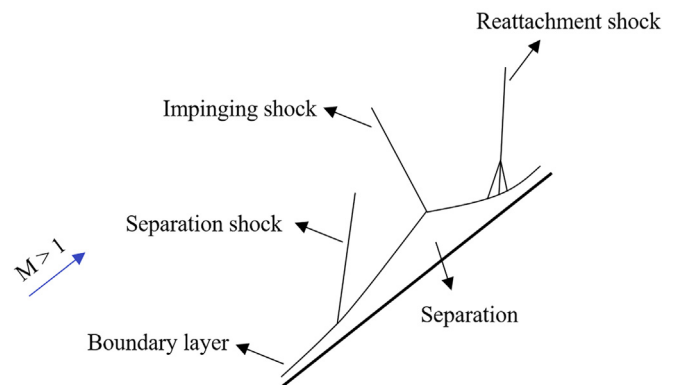**FIG. 4.** Compression corner recirculation bubble and shock wave system.

FIG. 5. Shock wave system in the case of boundary layer separation due to shock impingement on the surface.

V. NONEQUILIBRIUM SHOCK INTERACTION MECHANISMS

This section presents a parametric study of nonequilibrium shock structures with respect to the angle of the aft wedge. Numerical results are obtained on the basis of the two-temperature model introduced in Sec. II. Figure 6 shows the numerical schlieren for the four different geometries at the left, as well as pattern schematics that identify the flow features observed and help better understand the interaction mechanisms. Figure 7 shows a comparison of the respective surface pressure (left) and heat flux (right) distributions. For the first aft wedge angle of 40°, a type VI Edney pattern occurs at point P, where the interaction of oblique shocks generates another oblique shock curved shock (CS), a contact discontinuity (CD), and an expansion wave (EW), which reflects on the surface on the aft wedge, refracting on CD and causing CS to turn downward and becoming a curved shock. Upstream of point P, the system of waves depicted in Fig. 4 originates in the compression corner. Shocks DS and reattachment shock (RES) intersect each other before interacting with the leading shock (LS). However, this intersection occurs so close to the triple-point P that no other features are generated and the resulting pattern is basically equivalent to having all the three shocks interacting at point P, as illustrated in the schematic. The different flow features of this interaction pattern are also seen in the distribution of surface loads shown by the black curve in Fig. 7. An initial increase/decrease in pressure/heat flux occurs as a consequence of flow separation on the surface of the first wedge. Downstream of this region, both distributions are qualitatively similar, exhibiting a relatively wide peak that corresponds to the region of flow compression and reattachment to the wall on the surface of the second wedge. This is followed by a gradual decrease in pressure and surface heating resulting from the reflection of the expansion wave (EW) on the wall.

Increasing the aft wedge angle to 45° leads to a few changes in the shock interaction pattern over the double-wedge. The system of waves in the compression remains the same, but a significantly larger recirculation region is obtained. In this case, the stronger detachment shock (DS), characterized by a larger shock angle, intersects the leading shock (LS) much before reaching point P. This intersection locally generates a secondary type VI interaction pattern, exhibiting the typical expansion wave EW1 and contact discontinuity CD1 emanating from the intersection point. Downstream of this point, CD1 turns upward upon crossing the reattachment shock (ReS). Furthermore, the curved shock resulting from the secondary type VI interaction intersects the reattachment shock (ReS) at the triple-point P, which generates the additional features CS, CD2, and EW2 that characterize the primary type VI interaction pattern. Since all the differences in the interaction pattern occur away from the wall, the distributions of surface quantities is qualitatively very similar to the previous geometry, as expected. A quantitative comparison confirms the observation already made for the size of the separated region. Indeed, we can see in Fig. 7 that for this geometry the flow separates at $x = 0.135$ m, whereas for the 40° aft angle the separation point is located at $x = 0.165$ m. The higher aft wedge angle leads to an overall stronger shock structure, with a peak of pressure and heat flux resulting from the reattachment of the boundary layer, that is, respectively, 16% and 21% larger for this case.

For the 15°–50° geometry, the boundary layer separates closer to the leading edge and the size of the recirculation bubble further

enlarges. In the vicinity of the compression corner, a system of waves equivalent to the one found for the previous test-case is obtained, with a local type VI interaction originating at point Q as a result of the intersection between the leading shock (LS) and the detachment shock (DS). Further downstream, the boundary layer gradually reattaches accompanied by a series of compression waves that merge, forming the reattachment shock (ReS). The flow pattern generated in the vicinity of the second wedge corresponds to a type V with a regular reflection configuration, which significantly differs from the ones observed up to this point. The curved shock resulting from the type VI interaction and the bow shock (BS) interact at the triple-point P, from which a transmitted shock (TS) emanates. The latter intersects with shock ReS in a regular refection that gives rise to the reflected shocks RS1 and RS2. Shock RS1 reflects on the contact discontinuity CD2—arising from the shock interaction at point P—and an expansion fan EW3 forms, accelerating the flow. Upon this reflection, CD2 changes its direction because of the increased pressure behind the shock wave, and a convex corner is formed. Further downstream, EW3 reflects on the surface of the second wedge and crosses CD2. The contact discontinuity CD1 generated in the type VI interaction plays an active role in the mechanism of the type V interaction. After crossing the reattachment shock (ReS), turning it upward and generating another expansion wave EW2, it intersects shock RS2. From this latter interaction, CD1 changes its direction and ends up merging with CD2. The relatively weak shock RS2 further loses its strength when crossed by CD1 and the SBLI of shock RS2 on the surface of the second wedge is weak, never causing the boundary layer to separate. The increased complexity of the flow pattern obtained for this geometry is also reflected on a qualitatively different behavior of the surface pressure and heat flux distribution. For this case, after the first peak caused by reattachment of the boundary layer, both pressure and heat flux drop as a consequence of the expansion wave EW2 that reaches the surface of the second wedge. A second peak, 12% and 23% lower in pressure and heat flux, respectively, is observed just after, resulting from the weak impingement of shock RS2 on the surface.

As the aft wedge angle is further increased to 55°, the trend previously observed for the location of the separation point and size of the corresponding recirculation bubble holds. This trend can be easily seen in Fig. 7(a), shown by the location of first increase in pressure, corresponding to the detachment shock. Overall, the shock interaction mechanism obtained for this test-case is similar to the one obtained for 50°. The increased angle of the detachment shock (DS) and stand-off distance of the bow shock (BS) leads to a stronger shock TS emanating from the triple-point P. The main differences in the flow pattern arise from the higher angle of shock RS2. The impingement of the latter shock on the surface of the second wedge leads to a stronger SBLI, which in this case results in localized boundary layer separation. Similar to what occurs in the compression corner, this separation is accompanied by an additional detachment shock DS2 and reattachment shock ReS2 that increase the complexity of the wave system. Both of these shocks end up reflecting on the contact discontinuity CD2 in a regular manner. In Fig. 7(a), the several stages of flow compression are shown, corresponding to detachment and reattachment of the boundary layer in the compression corner, followed by detachment and reattachment of the boundary layer in the region of shock impingement. These four successive shocks cause the surface pressure to rise much above the previous cases, with a peak that is 54% larger
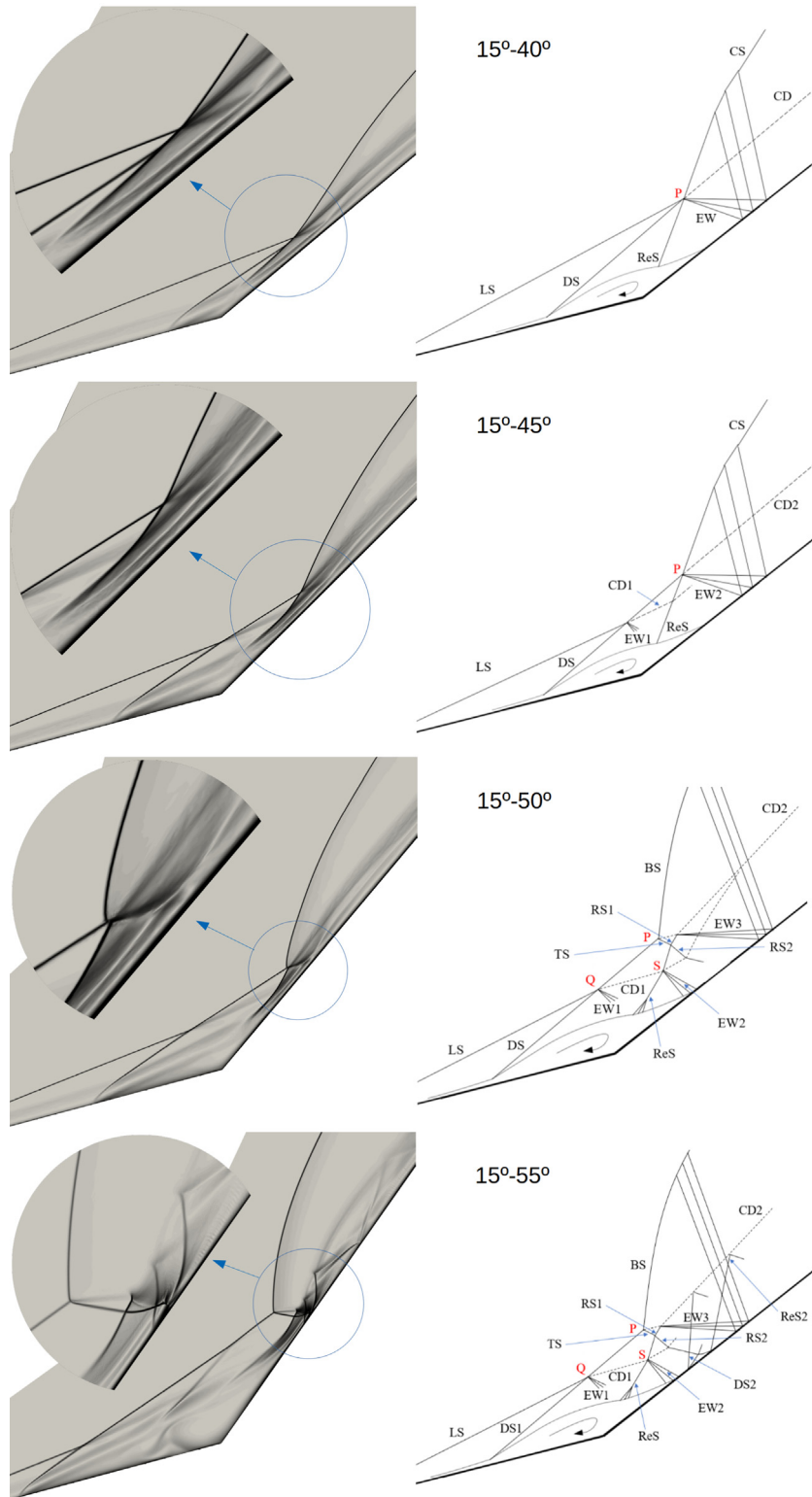
FIG. 6. Numerical schlieren (left) and schematics (right) for shock interaction patterns obtained with a two-temperature model.
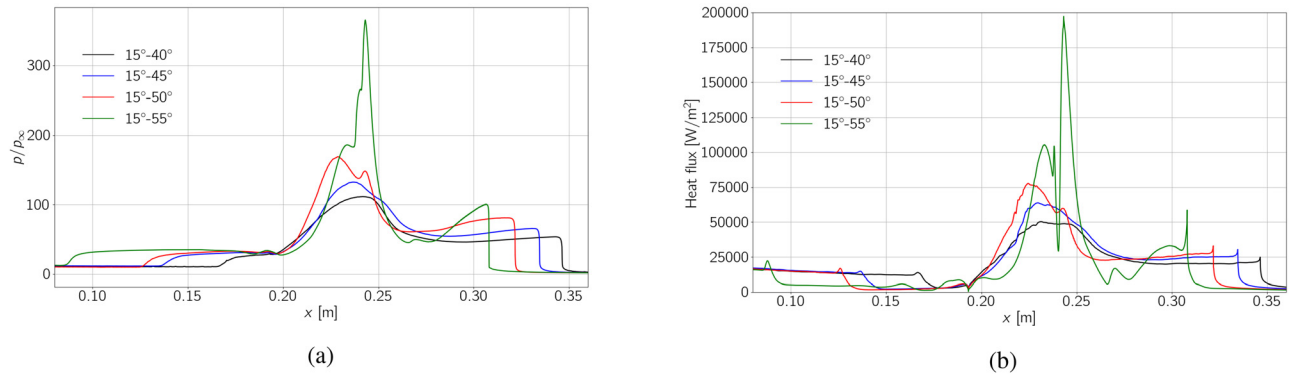
FIG. 7. Comparison of surface aerothermal loads obtained with a two-temperature model for the different double-wedge geometries: (a) normalized pressure distribution and (b) heat flux distribution.

than the one for the 15°–50° geometry. The larger separation region in the compression corner contains some vortex dynamics that can be seen in the heat flux surface distribution. This dynamics is seen in Fig. 7(b) between $x = 0.15$ m and the compression corner at $x = 0.193$ m, where some fluctuations of the surface heating occur. Downstream of the compression corner, the heat flux gradually rises as a consequence of the reattaching boundary layer, generating a relatively wide peak at $x = 0.233$ m. The following narrow peak occurs as a result of the detachment shock DS2, followed by a drastic drop corresponding to the boundary layer separation induced by impingement of shock RS2. Upon reattachment, accompanied by shock ReS2, the boundary layer becomes extremely thin and the pressure is high, leading to very localized strong surface heating of about 197 000 W/m², 61% higher than the maximum obtained for the 50° aft wedge angle.

A. Thermal nonequilibrium effects

The presence of nonequilibrium phenomena is explicitly discussed in this section. The maximum flow temperature of 2621 K was observed for the highest aft angle of 55° as expected, just behind the strongest portion of the bow shock. No changes of mass fraction were seen for any of the cases, indicating that there was no dissociation being activated. Since for the geometries and conditions studied the flow is chemically frozen, the focus is exclusively on the effects of vibrational excitation. Figure 8 shows a measure of the degree of thermal nonequilibrium in the flow (difference between trans-rotational and vibro-electronic temperatures) obtained for all geometries. It is evident that for all different aft angles, the state of thermal equilibrium of the freestream is not preserved after the shocks. Right behind the leading shock (LS), the vibrational temperature starts to rise, but remains below the translational temperature due to the vibrational relaxation time that it takes to equilibrate the two internal modes of energy. Regions of stronger nonequilibrium take place behind the strongest portion of the bow shock, since these are the regions where a larger amount of kinetic energy is transformed into internal energy. As the aft angle increases, the bow shock is stronger and so is the thermal nonequilibrium in this region. However, larger regions of thermal equilibrium are seen also as the angle increases. This is because post-shock velocities are lower for stronger shocks, therefore the flow residence time increases and becomes much larger than vibrational

relaxation time. This same reasoning would explain why the conclusions of this paper differ from the one drawn by Candler,[14] who observed a very small region with thermal nonequilibrium in their results. The degree of nonequilibrium established in supersonic/hypersonic flows may vary substantially from case to case, depending on the different parameters. The different geometrical shape used by Candler (cylinder) and larger freestream Mach number studied in his work result in a much stronger bow shock, associated with much larger post-shock translational temperatures (on the order of 10^4). Following the reasoning above, it is expected that, in that case, equilibration of internal energies is achieved much faster and therefore a smaller region of the flowfield is in thermal nonequilibrium.

Furthermore, thermal equilibrium tends to be reached in other regions of low velocity such as separated regions, either in the recirculation bubble in the vicinity of the compression corner—except for the lowest angle where this bubble is too small—or regions of separation due to shock impingement on the surface of the second wedge. On the other hand, downstream of the expansion corner, the vibrational temperature becomes higher than the translational one. This is a state of population inversion in the vibrational levels, where the upper states are more populated than the lower ones. The rapid expansion causes the translational energy to suddenly decrease below the vibrational one, which is a state of thermal nonequilibrium that is opposite of what occurs behind a shock wave. It is evident for all test cases that vibrational degrees of freedom are excited for the given flow conditions, and that they are not in equilibrium with the translational energy.

VI. COMPARATIVE STUDY WITH DIFFERENT MODELS

In order to assess the role of thermal nonequilibrium on the physics of shock interactions obtained with the two-temperature model, the same test-cases have been simulated with the simplified models introduced in Sec. VI A. The aim is to assess the differences of shock structures numerically obtained with the equilibrium models in relation to the more detailed two-temperature model. Both qualitative and quantitative comparisons are reported to understand the impact of different simplifying assumptions on the characteristics of the flow in terms of interaction patterns as well as surface pressure and wall heat flux distribution, respectively. For simplicity, hereinafter the perfect ideal gas model is referred to as PIG, the thermally perfect gas
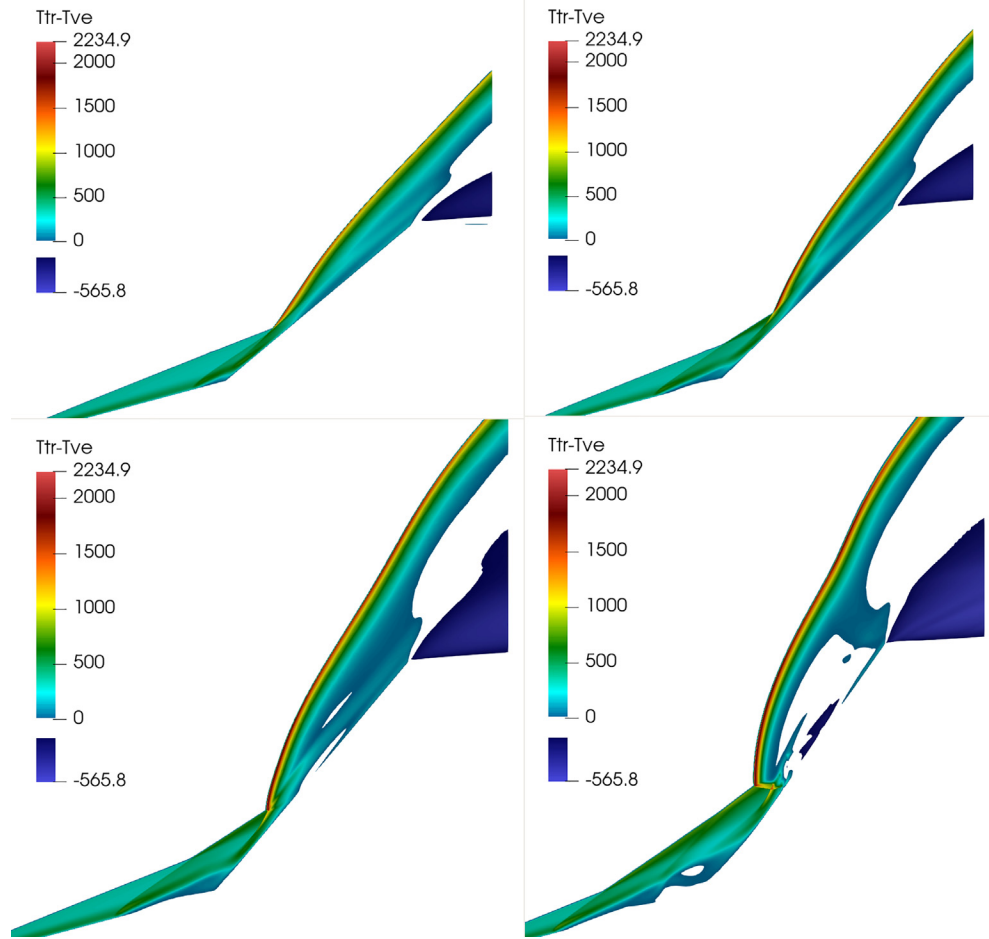
FIG. 8. Degree of thermal nonequilibrium obtained for all geometries: $15°–40°$, $15°–45°$, $15°–50°$, and $15°–55°$ double-wedge.

model as TPG and the two-temperature nonequilibrium model as NEQ.

A. Models assuming equilibrium

The system of equations implemented for the perfect ideal gas and for the thermally perfect gas models follows the widely known classical Navier–Stokes approach for a continuum, viscous laminar, chemically frozen flow in thermal equilibrium, with a single equation for the energy (total energy of the mixture) and assuming a single temperature T. In both models, the specific heats are defined as

$$C_p = \frac{\gamma R}{\gamma - 1}, \quad C_v = C_p - R, \tag{23}$$

where C_p is the specific heat of the mixture at constant pressure, C_v is the specific heat of the mixture at constant volume, $\gamma = \frac{C_p}{C_v}$ is the ratio of specific heats, and R is the gas constant of the mixture. In the perfect ideal gas model, there is no physical modeling of the internal structure of molecules in the gas. It is considered that rotational/vibrational/electronic degrees of freedom are not excited and therefore rotational/

vibrational/electronic energy is not accounted for. Internal energy is only described in terms of translational degrees of freedom. The specific heats, and therefore the ratio of specific heats, remain constant with temperature.

The thermally perfect gas model considers the impact of vibrational excitation assuming thermal equilibrium. As the internal energy of the gas increases, a portion of it is instantaneously transferred from the translational to the vibrational mode, instead of raising the temperature of the gas. This results in a decrease in the specific heat ratio with temperature $C_p = f(T)$ and $C_v = f(T)$, which depends on the mixture in question. The temperature at which this process becomes significant depends on the characteristic vibrational temperature of the molecules. As shown in Fig. 9, for the mixture studied in this work, this model predicts a significant decrease in the specific heat ratio up to 2000 K, above which this change becomes more gradual. The graph shows that the low characteristic vibrational temperature of CO_2 molecules has a large impact on the thermodynamic properties of the mixture even if thermal nonequilibrium is not considered, and therefore is it expected that this will influence the shock structures of the flows studied in this paper.
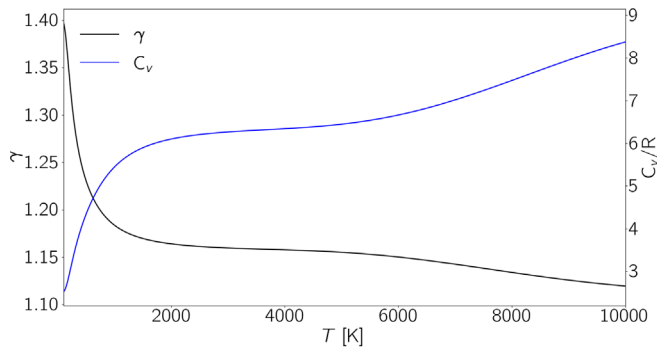
FIG. 9. Variation of specific heat at constant volume C_v and specific heat ratio γ of a CO_2:0.97, N_2:0.03 mixture with temperature for a thermally perfect gas model.

B. 15°–40° double-wedge

Figure 10 shows the numerical results obtained for density gradient in the case of the 15°–40° geometry, as well as corresponding auxiliary schematics of the shock interaction pattern. A type VI Edney pattern occurs at point P for all three models. However, upstream of point P, all models result in different shock structures originating at the compression corner. Both the PIG and NEQ models exhibit the system of waves depicted in Fig. 4, where the major difference arises from the different locations of the detachment shock (DS). In the case of the PIG model, a larger separation region leads to a shock DS that crosses the leading shock (LS) before reaching point P, leading to a secondary type VI pattern associated with the contact discontinuity CD1 and expansion wave EW1. EW1 impinges on the slip layer surrounding the separation bubble and CD1 refracts on the shock wave

arising from the reattachment of the boundary layer, reflected shock (RS). For the PIG model, the primary type VI pattern is a result of interference between ReS and the curved shock generated in the secondary type VI interaction. On the other hand, for the NEQ model, the more downstream location of the detachment shock (DS) keeps it under the leading shock. The simplest shock structure is observed when a TPG model is used. In this case, the boundary layer separates very slightly (the separation is too small to be visualized in the density gradient plots) and no reattachment shock is generated. The interaction pattern observed in this case is purely due to the interaction between shocks LS and DS. It is fair to conclude that the differences between the obtained shock interaction patterns originate from the different sizes of the recirculation bubble in the compression corner. For the PIG model, the internal energy of the gas—which is increased through a shock wave, as a result of the conversion of kinetic energy in the form of flow velocity to internal energy in the form of temperature and pressure—is stored only in the translational degrees of freedom, causing a stronger disturbance of the flow associated with a larger separation, than for a case where vibration excitation is accounted for. The TPG and the NEQ models, on the contrary, account for the partition of internal energy between different internal energy modes, therefore resulting in lower post-shock temperatures and increased densities associated with a smaller recirculation bubble. The detailed NEQ model explicitly models this relaxation process by accounting for the time that it takes for the energy transfer to reach a state of equilibrium. Right behind the shock wave, vibrational levels are not populated instantaneously, which means that the portion of kinetic energy of the flow that is transformed into internal energy across the shock is stored only in the trans-rotational degrees of freedom at first, and then gradually transferred to the vibro-electronic modes. In the TPG model,
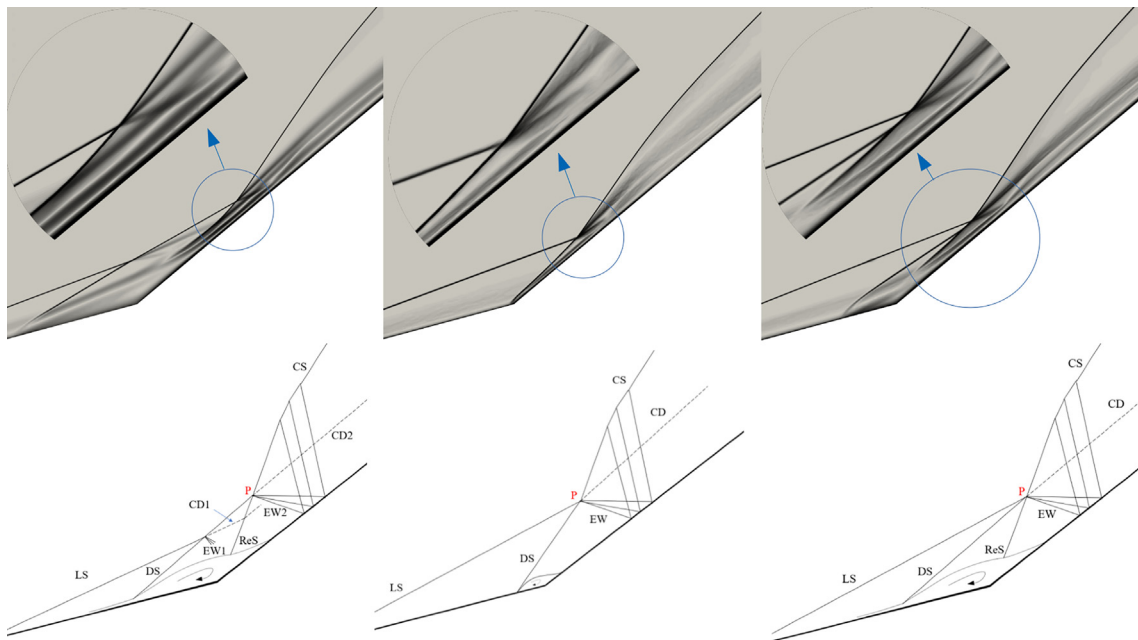

FIG. 10. Comparison of density gradients and shock interaction schematics obtained for a CO_2–N_2 flow over the 15°–40° double-wedge: perfect ideal gas (left), thermally perfect gas (middle), and nonequilibrium gas (right).

the influence of vibration is modeled in a simplistic way, where the same portion of energy is redistributed instantaneously among the trans-rotational and vibro-electronic modes. As a consequence, the effect of energy absorption by vibrational excitation is further enhanced and almost no separation occurs. For the flow to deflect in the same direction, weaker disturbances are obtained when more energy is absorbed by the vibrational modes.

Figure 11 shows the normalized pressure and wall heat flux for the surface of the $15°$–$40°$ double-wedge. Despite the different interaction patterns obtained for the three models, the profile of both surface quantities is qualitatively similar. The LS post-shock pressure is almost identical for the PIG and NEQ models, higher than for the case of the TPG model, which exhibits a more attached shock in the nose. The first increase in pressure corresponds to the separation of the boundary layer, which occurs earlier for the PIG model at $x = 0.135$ m, then for the NEQ model at $x = 0.168$ m, and nearly at the compression corner at $x = 0.192$ m for the TPG model. The precise locations of the separation point for each model are depicted in Fig. 11(b), indicated by green arrows. The larger values of pressure, corresponding to the peaks, occur in the reattachment region for all models. It is interesting to notice that, despite the overall tendency for a more complex interaction in the case of the PIG model, the more gradual reattachment of the recirculation bubble leads to a wider and 12% lower pressure peak for this model, whereas the NEQ and TPG models are almost identical in the maximum value, with a delayed location for the NEQ model, as expected from the larger size of the separated region. The different sizes of the recirculation bubble can also be clearly seen in Fig. 11(b), in the regions where the wall heat flux is the lowest for each case. From the blue line, it is now evident that an extremely small separation exists in the compression corner of the TPG model, shown by the spike of minimum heat flux at about $x = 0.19$ m. The smoother separation obtained in the PIG solution is accompanied by a separation shock of a smaller angle than for the TPG and NEQ models, for which separation of the boundary layer is more abrupt. As such, the stronger separation shocks of the latter models locally compress the flow against the wall, leading to small spikes of the heat flux in these regions. As the boundary layer reattaches, a region of high local aerodynamic heating occurs. In the case of the TPG model, the separation region is quite small and reattachment occurs abruptly. This results in a larger heat flux peak, of about 17% higher than for the NEQ model

and 44% higher than for the PIG model, where reattachment takes place gradually. The monotonic behavior observed for the peaks of heat flux follows the thickness of the thermal boundary layer obtained for each model. When vibrational excitation is not accounted for (PIG model), a thicker boundary layer is obtained since the post-shock temperature is higher than the translational temperature resulting from the vibrational nonequilibrium solution (NEQ model), due to the gradual absorption of internal energy by the vibrational degrees of freedom of the molecules in the latter case. In turn, the NEQ post-shock translational temperature is higher than the temperature obtained for the equilibrium solution (TPG model), for which the partition of energy between the two degrees of freedom is modeled to occur instantaneously. Apart from the higher heat flux peak obtained for the TPG model relative to the NEQ model, the locations and values of the heat flux peaks in the reattachment region follow the tendency observed in the pressure plots. For all three solutions, the expansion fan that forms at the ending point of the second wedge causes a sudden drop in surface pressure and heat flux.

C. $15°$–$45°$ double-wedge

Figure 12 shows density gradient contours for the $15°$–$45°$ geometry and the schematics corresponding to the obtained shock patterns. As opposed to the NEQ model, for the PIG and TPG models the increment of $5°$ in the aft wedge angle is not sufficient to change the interaction pattern that was observed in the case of the $15°$–$40°$ double-wedge. The system of waves remains identical, with the differences lying in the size of the recirculation region, the shock angles, and the curvature of the bow shock CS. For the PIG case, the separation point occurs closer to the leading edge for the $15°$–$45°$ geometry than for the $15°$–$40°$ geometry, at $x = 0.10$ m vs $x = 0.13$ m, respectively, which results in a significantly larger separated region and larger angle for the detachment shock (DS). Additionally, the $45°$ aft wedge angle leads to a reattachment shock (ReS) and an interaction region that is further from the wall and in a more downstream location. The bow shock CS follows this tendency as well, being slightly more curved and significantly more detached from the surface of the second wedge. When it comes to the TPG model, the increment in wedge angle also influences the separation region in the compression corner. For this geometry, a small detachment of the boundary layer can already be
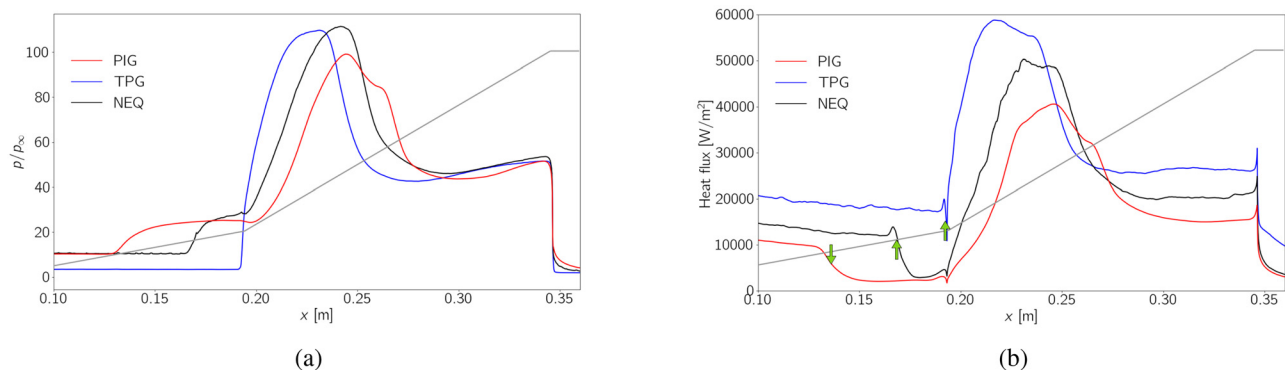

FIG. 11. Comparison of surface aerothermal loads of (a) normalized pressure and (b) heat flux, for the $15°$–$40°$ double-wedge: perfect ideal gas, thermally perfect gas, and nonequilibrium gas model.
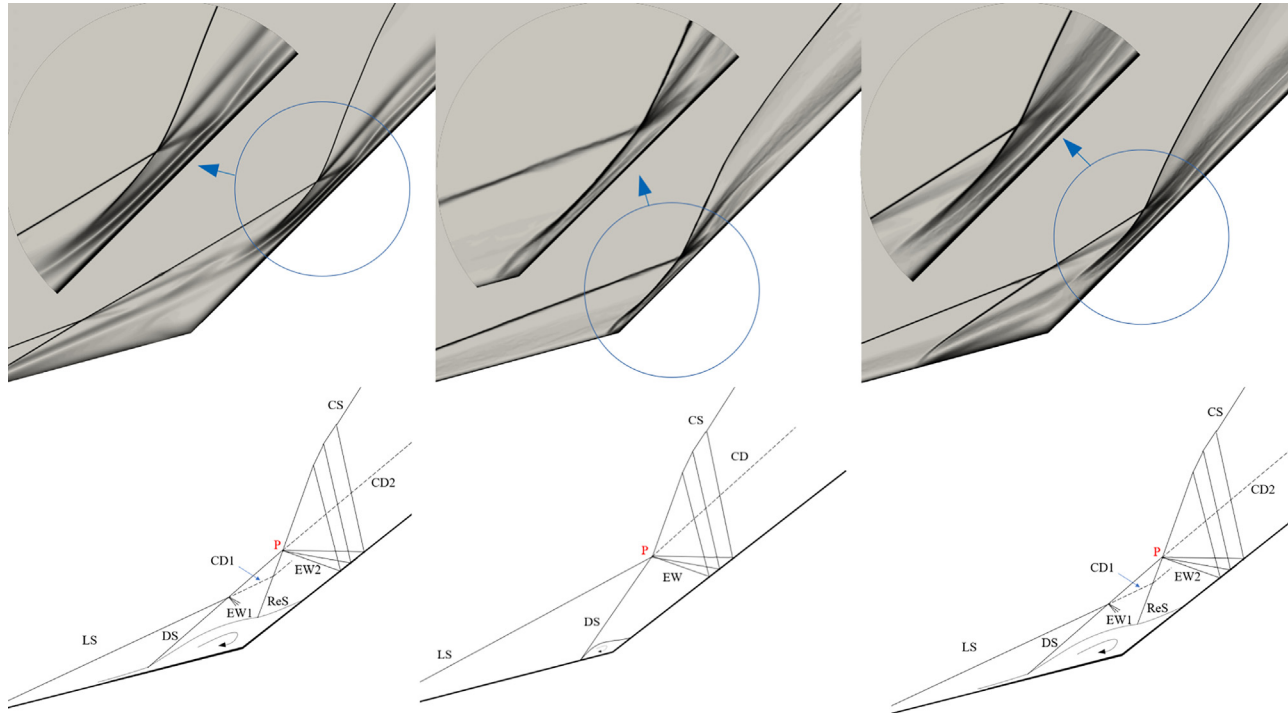
FIG. 12. Comparison of density gradients and shock interaction schematics obtained for a CO_2–N_2 flow over the $15°$–$45°$ double-wedge: perfect ideal gas (left), thermally perfect gas (middle), and nonequilibrium gas (right).

visualized. Even though a reattachment shock does not form, a small compression wave occurs in this location and turns the detachment shock (DS) downward, making it more attached to the wall. Contrary to what is observed for the PIG model, this causes the interaction region to shift upstream, even though the CS shock layer is slightly larger. It is relevant to note that, for the PIG model, the angle of the aft wedge is the only parameter that changes from test-case to test-case, which means that all the differences in the flowfield are solely attributed to this factor. For the TPG and NEQ solutions, the thermodynamic properties of the mixture also play a role. The fact that vibrational excitation absorbs the translational energy of the flow, reducing the post-shock temperatures and increasing the density, leads to smaller shock standoff distances and overall weaker shock interactions. Accordingly, in the TPG solution, where the impact of energy absorption by vibration is expected to be more significant, the shock interaction pattern changes the least. In the case of the NEQ model, where the influence of vibrational excitation is expected to be smaller than for the equilibrium solution due to the associated time of relaxation toward equilibrium, the shock interaction pattern actually changes when the angle is increased, suggesting that the change in geometry has a larger impact on the flow physics than the real gas effects. This is also seen in Fig. 8, which shows that the degree of thermal nonequilibrium does not seem to be very different between the first two angles. The significantly larger separation length and the stronger detachment shock associated with a larger angle result in the local secondary type VI interaction found in the PIG solution for both $15°$–$40°$ and $15°$–$45°$ double-wedges.

Figure 13 shows the surface quantities obtained for the $15°$–$45°$ double-wedge. The surface pressure profiles are qualitatively similar to the ones obtained for the $15°$–$40°$ double-wedge, except for the fact that, in this case, the TPG model results in a 12% larger maximum value than that of the NEQ model. Additionally, the separated region is now evident for the TPG model, shown by the first spike resulting from the detachment shock (DS) and followed by a sudden drop due to the small separated region. As expected from the increase in angle of the aft wedge and its effects on the strength of the shocks, the separation lengths as well as pressure peaks are larger for all models. The same observations hold for the heat flux plots. The monotonic tendency observed in the peaks of both pressure and heat flux (TPG → NEQ → PIG models) follows the behavior of the reattachment of the boundary layer. The more internal energy is stored in the translational energy mode of the molecules of the gas, the larger recirculation regions are obtained. Larger recirculation regions are followed by a more gradual compression that reattaches the flow to the wall, therefore resulting in lower and wider peaks for the surface quantities. The impact of a slightly larger separated region for the TPG model in relation to the previous geometry is noticeable from the overshoot occurring around $x = 0.19$ m, which corresponds to the detachment shock (DS). The very short separated region in the compression corner results in undershoot right downstream.

D. $15°$–$50°$ double-wedge

Figure 14 shows the same set of numerical results for the $15°$–$50°$ geometry. It is evident that for all the three models, completely
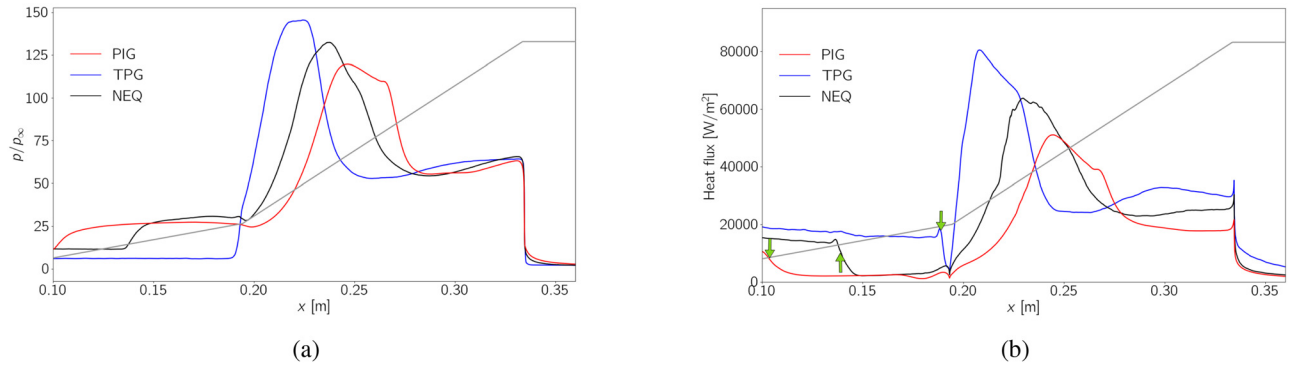
FIG. 13. Comparison of surface aerothermal loads of (a) normalized pressure and (b) heat flux, for the 15°–45° double-wedge: perfect ideal gas, thermally perfect gas, and nonequilibrium gas model.

different shock interactions patterns are obtained by incrementing 5° in the aft wedge angle. All the three shock interaction mechanisms exhibit instead a type V pattern with a regular reflection configuration. The trend observed for previous aft angles when it comes to the different ways of modeling the behavior of vibrational relaxation is maintained: the more internal energy is absorbed in the excitation of the vibrational modes, the smaller is the size of the recirculation bubble and separation length, the less complex is the overall interaction pattern (PIG → NEQ → TPG). Compared to the previous geometries, stronger SBLI occurs, as there is shock impingement on the wall of the second wedge. As opposed to the NEQ solution, the boundary layer obtained with the PIG model separates very close to the leading edge [see separation point in Fig. 15(b)], creating a very large separation bubble inside which vortex dynamics occurs. The type VI interaction resulting from the intersection between shocks LS and DS is also seen in the PIG solution, but for this case it occurs in the vicinity of the
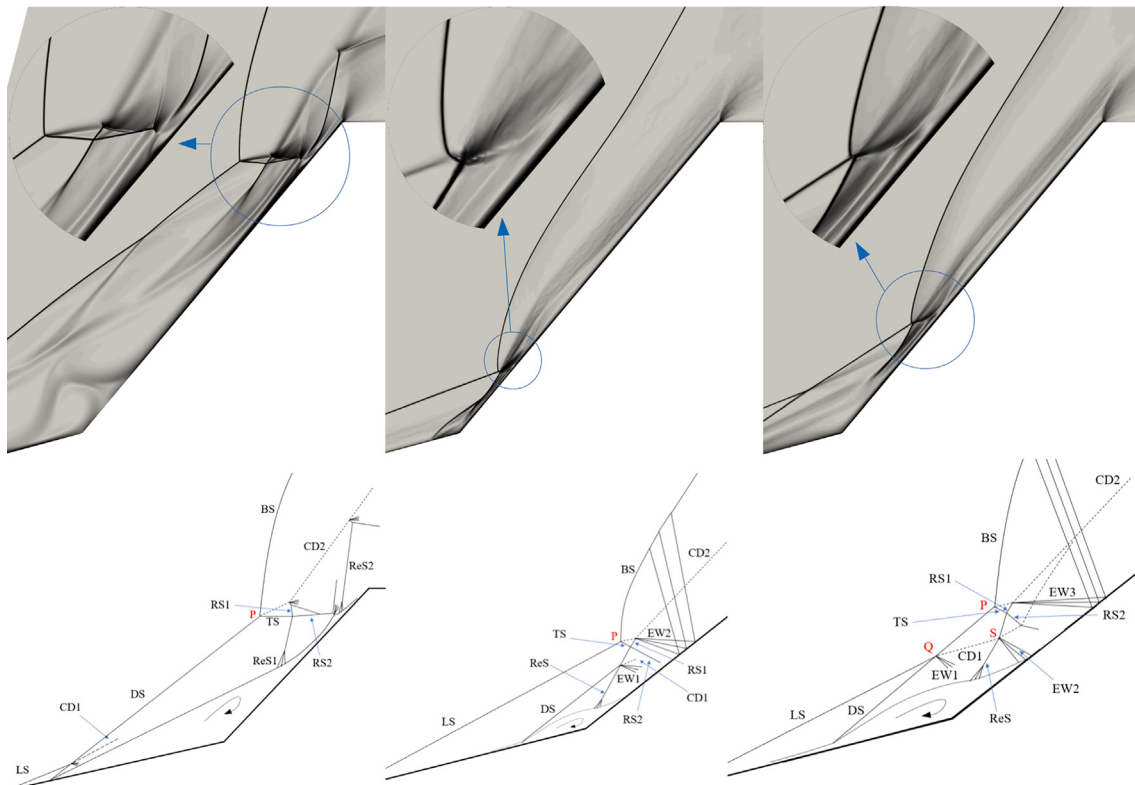

FIG. 14. Comparison of density gradients and shock interaction schematics obtained for a CO_2–N_2 flow over the 15°–50° double-wedge: perfect ideal gas (left), thermally perfect gas (middle), and nonequilibrium gas (right).
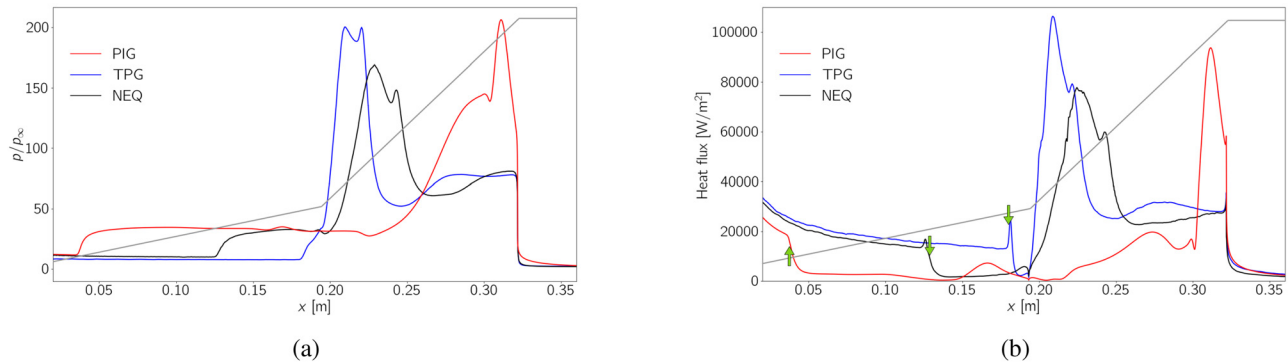
FIG. 15. Comparison of surface aerothermal loads of (a) normalized pressure and (b) heat flux, for the 15°–50° double-wedge: perfect ideal gas, thermally perfect gas, and nonequilibrium gas model.

leading edge. The contact discontinuity CD1 ends up being dissipated in the interaction with the separated viscous layer and the vortexes generated inside the recirculation bubble, never reaching the region where the main interaction takes place. Shocks TS and ReS1 interact in a regular reflection that gives rise to a wave system similar to the one seen in the NEQ solution. However, for the PIG model RS1 impinges on the contact discontinuity CD2 in a lambda-shaped stem reflection, resulting in a small expansion and an additional shock that impinges on RS2. While for the NEQ case, shock RS2 impinged on the surface of the second wedge in a relatively weak manner, here the adverse pressure gradient leads to a clear SBLI. Shock RS2 causes the boundary layer to locally separate and reflects in a Mach stem (MS) inverted lambda-shaped pattern. Downstream of the normal shock impinging on the wall, the reattachment of the boundary layer is accompanied by a series of compression waves that merge into the reattachment shock ReS2, which in turn reflects on the contact discontinuity CD2 in another Mach reflection structure. Compared to the NEQ results, the TPG solution is characterized by a much smaller separated region, as well as a significantly weaker detachment shock (DS) that never crosses the leading shock (LS). Accordingly, a local type VI interaction occurs between DS and ReS and point P marks, instead, the interaction between the leading shock (LS), the transmitted shock (TS), and the bow shock (BS). The resulting contact discontinuity CD1 refracts on shock RS2, which impinges on the wall of the aft wedge without separating the boundary layer.

Figure 15 shows the surface aerothermal loads for the 15°–50° double-wedge. As expected from interaction patterns discussed above, the PIG solution results in a wall normalized pressure and heat flux distribution that are qualitatively very different from the ones obtained for the models that account for vibrational excitation. After the plateau region of pressure in the separated region, a gradual increase translates the smooth reattachment of the boundary layer. Once the boundary layer is reattached, a strong peak of pressure emerges due to the impingement of shock RS2 on the surface of the aft wedge. It is noticeable that, for this case, the main shock interaction mechanism occurs very close to the expansion corner. On the other hand, the TPG and NEQ models result in surface distributions that are qualitatively very similar. Downstream of the separated region, which is much smaller for the TPG solution, both curves display two peaks of pressure, respectively, due to the reattachment of the boundary layer and

impingement of shock RS2. In the NEQ solution, the flow expands downstream of boundary layer reattachment, resulting in a impingement peak of pressure which is about 12% lower than the one caused by reattachment. For the TPG model, reattachment and shock impingement occur close together, therefore the flow does not expand significantly before compressing again and the two peaks have a very similar intensity of about 200. For both models, after the strong expansion downstream of the second peak, the movement of the contact discontinuity toward the wall slightly recompresses the fluid before reaching the convex expansion corner. As observed for the previous geometry, the smaller recirculation bubble of the TPG solution leads to a higher and thinner peak of pressure, revealing a stronger recompression in the reattachment region. as opposed to the NEQ solution, for which a gradual reattachment results in a lower and wider peak. The heat flux distribution of the TPG and NEQ models fairly follow what is seen in the pressure plot, except for the second heat flux peak of the TPG model, which is 25% lower than the first one. This is due to the fact that shock RS2 crosses the thermal boundary layer and further weakens, which would affect the heat flux but not pressure. When it comes to the PIG model, downstream of the separation point and up to about $x = 0.26$ m, the region of separation exhibits fluctuations of heat flux that take place as a consequence of the vortexes that result from flow recirculation. Occurrence of vorticity beneath the separation line due to increasing aft angle has been reported before.[3,4] Between $x = 0.25$ m and $x = 0.29$ m, a wide and low local peak occurs as a result of the smooth reattachment of the boundary layer. At $x = 0.29$ m, the heat flux slightly decreases again due to shock-induced separation. The boundary layer reattachment following the impingement of shock RS2 then leads to a very localized peak of heat flux at about $x = 0.31$ m, before the strong expansion occurring due to the convex corner.

E. 15°–55° double-wedge

As opposed to the NEQ model, the flow over the 15°–55° geometry using a PIG model did not reach a steady state, therefore the solution obtained with the steady state solver was provided as a first guess to resolve the unsteady shock interaction process with time-accurate simulations. Figure 16 shows density gradient contours and shock pattern schematics for the different shock structures that were obtained. The complexity of this test-case deserves a thorough description of the unsteady dynamics driving the mechanism of interaction. The flow
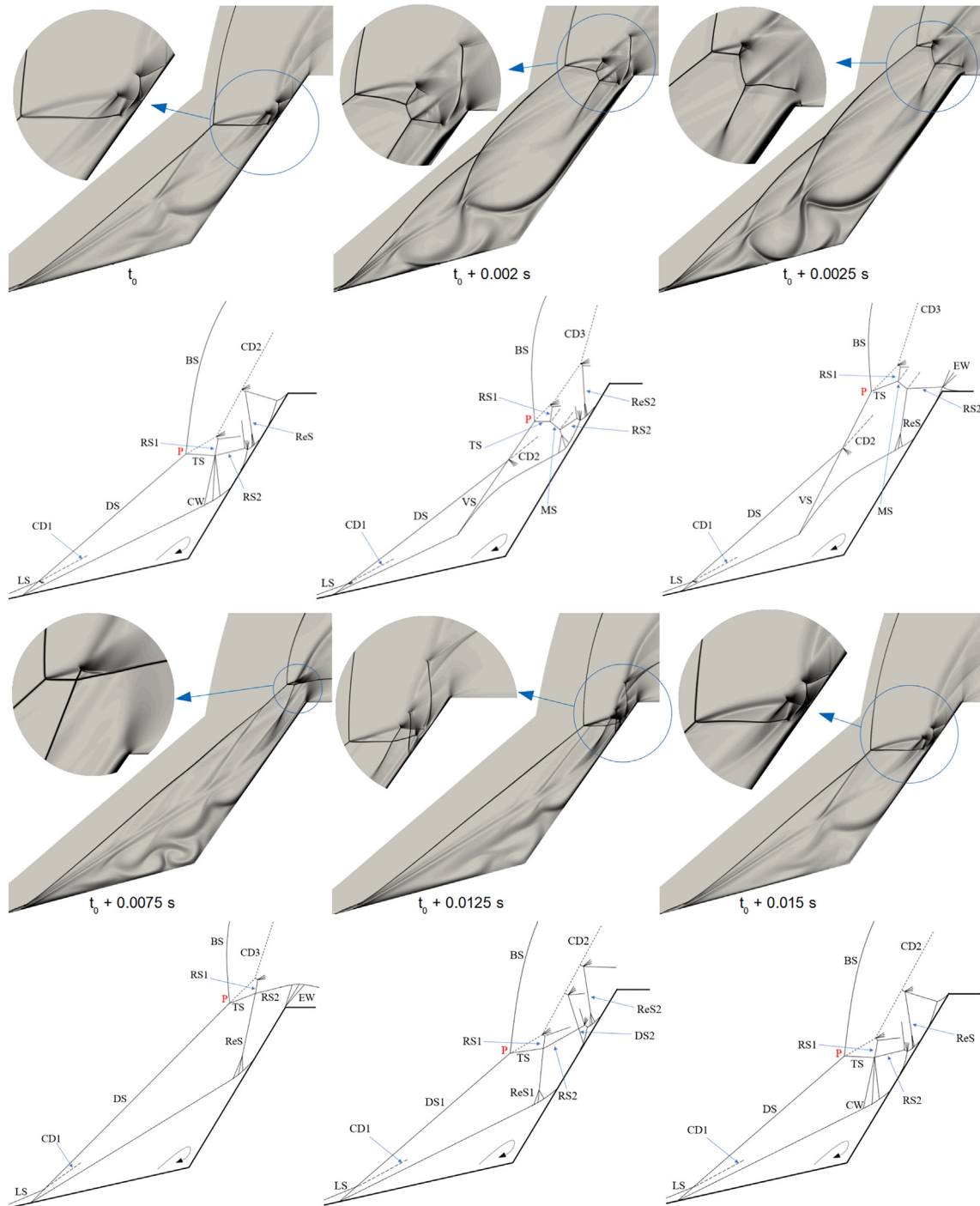
FIG. 16. Unsteady density gradients and shock interaction schematics obtained for a CO_2–N_2 flow over the $15°$–$55°$ double-wedge with a perfect ideal gas model.

physics became periodic after 0.015 s, therefore the first and last snapshots show the same flowfield. The periodicity of the flow physics becomes evident in Fig. 17, which shows the instant normalized pressure and heat flux distributions for this test-case. The initial and final curves, respectively, at t_0 and $t_0 + 0.015$ s, are almost identical. Even though the heat flux profiles at these instants of time do not match with a perfect superimposition, the shock interference pattern does not change and the exact same type of interaction is obtained.
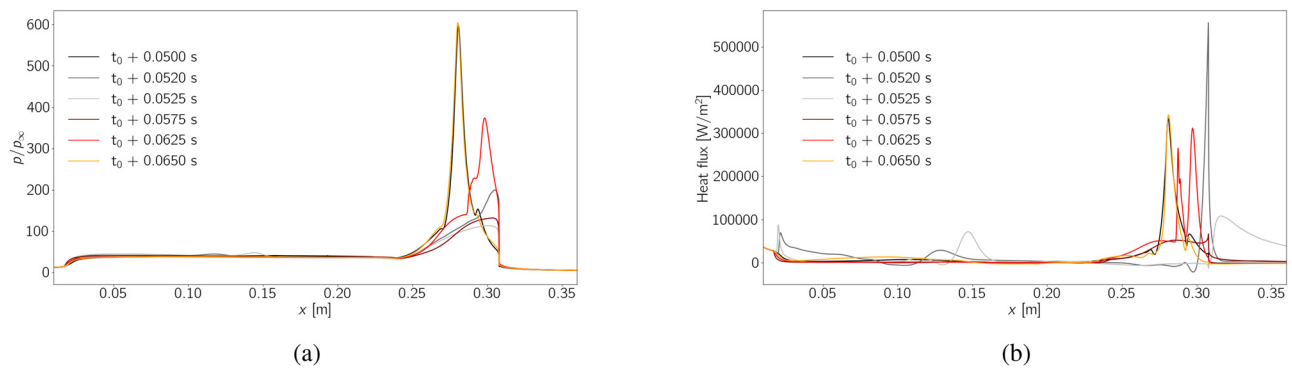
FIG. 17. Instant surface aerothermal loads for the 15°–55° double-wedge with a perfect ideal gas model: (a) normalized pressure distribution and (b) heat flux distribution.

At the initial instant of time t_0, the detachment shock (DS) interacts with the bow shock (BS) generated by the second wedge, forming a triple-point P with a transmitted shock (TS) directed toward the aft wedge. A second triple-point is formed as the reattachment compression wave (CW) interacts with the transmitted shock (TS). The shock interaction mechanism is quite similar to the one obtained for the 15°–50° geometry with a PIG model. The first difference lies in the fact that the compression wave (CW) generated in the reattachment of the boundary layer downstream of the compression corner does not form a shock wave before interacting with the transmitted shock (TS), but this does not seem to affect the overall type V interaction. Furthermore, when shock ReS reflects on the contact discontinuity CD2, in this case it impinges on the surface of the aft wedge, resulting in a third region of boundary layer separation and a spike in surface pressure and heating, at $x = 0.275$ m. The impingement of shock RS2 on the wall plays a major role in the unsteady mechanism of interaction. The shock-induced adverse pressure gradient is transmitted upstream through the subsonic portion of the boundary layer, affecting the overall shock system that becomes more complex at $t_0 + 0.002$ s. The propagation deforms the shear layer and significantly increases the size of the separation bubble in the compression corner, shifting the interaction region downstream. As seen in Fig. 17, the surface pressure peak has considerably decreased and is now located just upstream the expansion corner. On the other hand, the shock-induced separation leads to a minimum value of surface heating, just before a large spike due to reattachment of the boundary layer in this region. As the disturbances resulting from shock impingement travel upstream, vortex dynamics is generated/energized inside the large-scale flow separation, leading to the appearance of an additional shock wave vortex shock (VS), which interacts with the detachment shock (DS) in a local type VI interaction. The vorticity-related fluctuations of surface pressure and heat flux seen in Fig. 17 are an indicator of the upstream disturbances created by shock impingement. Even though the separation point on the fore wedge is never altered throughout the unsteady process, and the upstream conditions of the detachment shock (DS) do not change during the time-periodic flow, the strength of the detachment shock (DS) changes due to the variation of the separation angle. Reattachment of the large separation region is accompanied by a series of compression waves (CW) that, at this instant of time, merge to form a shock wave before interacting with shock TS. In an interaction

that is considerably stronger than for the previous instant of time, the reattachment shock and transmitted shock (TS) interact in a Mach reflection structure through the Mach stem (MS). From the extreme points of this Mach stem, two additional contact discontinuities emanate. Similar to what is observed in the previous snapshot, shock impingement of RS2 occurs further downstream on the surface of the second wedge. After impingement, RS2 is reflected on the surface on the aft wedge and then on CD2, at which point it becomes quite weak and ends up fading in the strong expansion of the convex corner.

At $t_0 + 0.0025$ s, the shock interaction mechanism has further shifted toward the expansion corner and maintains its structure. However, no shock impingement occurs at the wall of the second wedge, since RS2 only reaches the surface of the geometry downstream of the convex corner, where the strong expansion takes over. Meanwhile, the disturbances generated by previous shock impingement start damping out and decaying vortex activity causes shock VS to vanish and the angle and standoff distance of shock DS to decrease, as seen in the transition from $t_0 + 0.0025$ s to $t_0 + 0.0075$ s. Since shock DS strongly interacts with the bow shock (BS), the latter also gets closer to the wall. The interaction weakens, the two triple-points connecting the Mach stem collide and a type V pattern with regular shock reflection is formed. At this instant of time, the reattachment shock (ReS) and the transmitted shock (TS) reflect on each other in a regular manner, giving rise to shocks RS1 and RS2. The latter becomes curved when it interacts with the corner expansion fan, never reaching the wall. Accordingly, for these two instants of time, both surface pressure and heat flux do not exhibit any peaks upstream of the expansion corner.

At $t_0 + 0.0125$ s, the motion of the interaction mechanism has changed its direction and is moving upstream, as it becomes again more complex. A type V regular reflection still dominates the flow-field, but additional shock waves are formed. As the shock structure approaches its initial shape, some features are still different from the state of the flow at the start of the period. The reattachment region still exhibits a clear merging of the compression waves into a single shock ReS1, seen in Fig. 17(a) as the increase in pressure after the separation plateau. The following increase in surface pressure corresponds to the strong SBLI that results in a large shock-induced boundary layer separation. The size of the shock-induced separation is dictated by the impingement angle and strength of the transmitted shock. The

thickening of the boundary layer at this location further displaces the bow shock (BS) upstream along with the triple-point P. As a consequence of the larger separation, a detachment shock DS2, which is not seen at the first instant of time, appears upstream of the impingement location. In Fig. 17(b), this separation corresponds to the sudden drop in surface heating, located in between the two spikes generated at reattachment locations, ReS1 and ReS2. The reattachment shock ReS2 is also seen in the pressure plot as the peak of the red curve. The multiple shocks reflect on the contact discontinuity and the wedge surface, intersecting each other regularly. Finally at $t_0 + 0.015$ s, the shock structure has further moved upstream and its shape, as well as distribution of surface quantities, correspond to the ones obtained for the initial instant of time. The flow physics of this shock interaction mechanism can be summarized as a strong coupling between the separation angle, vortex dynamics in the separated region, the impingement of shock RS2, and overall shock structures.

Figure 18 shows the numerical results obtained for the 15°–55° double-wedge with the TPG and NEQ models. Accounting for molecular vibrational motion seems to stabilize the entire flow, since both of these solutions achieved steady state. In Ref. 11, it was stated that below a certain threshold value for the angle of the aft wedge, the flow reaches steady state after shock establishment time. Our results obtained for this geometry show that accounting for vibrational excitation delays this threshold. Given the trend observed in the parametric study, it is fair to assume that the equilibrium solution would lead to a later transition between a steady and an unsteady mechanism of interaction. In both cases, the increase in aft wedge angle in relation to the previous geometry leads to further displacement of the separation point toward the leading edge and a larger separation region (however still smaller than for the PIG solution). In the TPG solution, the pattern of interaction slightly changes in relation to the previous aft wedge angle. Shock DS has an angle that is large enough to cross the leading shock (LS). The shock wave system is equivalent to the one observed for the 15°–50° geometry with a NEQ model. However, now shock RS2 is strong enough to reflect on the surface of the second wedge, causing a small region of boundary layer separation. The interaction is overall stronger for the NEQ solution than for the TPG one. The increased angle of the detachment shock (DS) and standoff distance of the bow shock (BS) leads to a stronger shock TS emanating from the triple-point P, located further downstream than for the TPG model. This discrepancy also affects the intensities of the remaining shocks resulting from this interaction. The stronger reflection of RS2 on the surface of the second wedge leads to a stronger SBLI with a larger region of boundary layer separation that is accompanied by a detachment shock DS2 and a reattachment shock ReS2, which are not seen in the TPG solution.
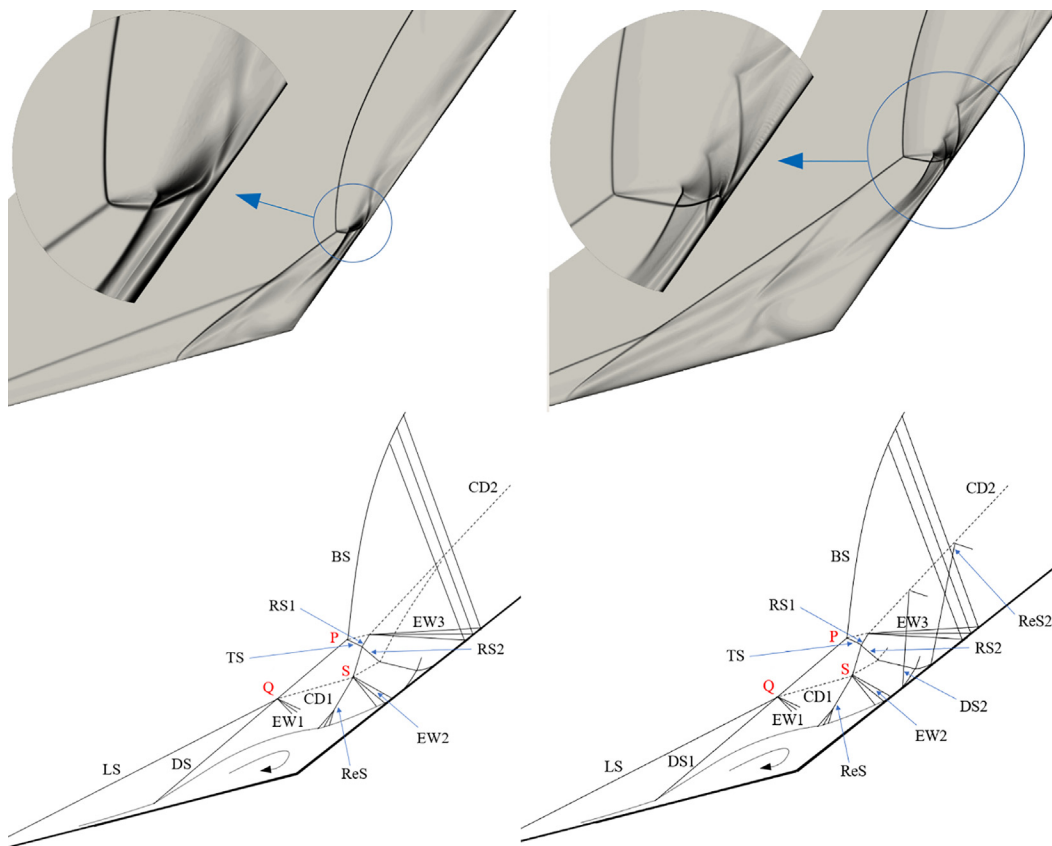

FIG. 18. Comparison of density gradients and shock interaction schematics obtained for a CO_2–N_2 flow over the 15°–55° double-wedge: thermally perfect gas (left) and non-equilibrium gas (right).
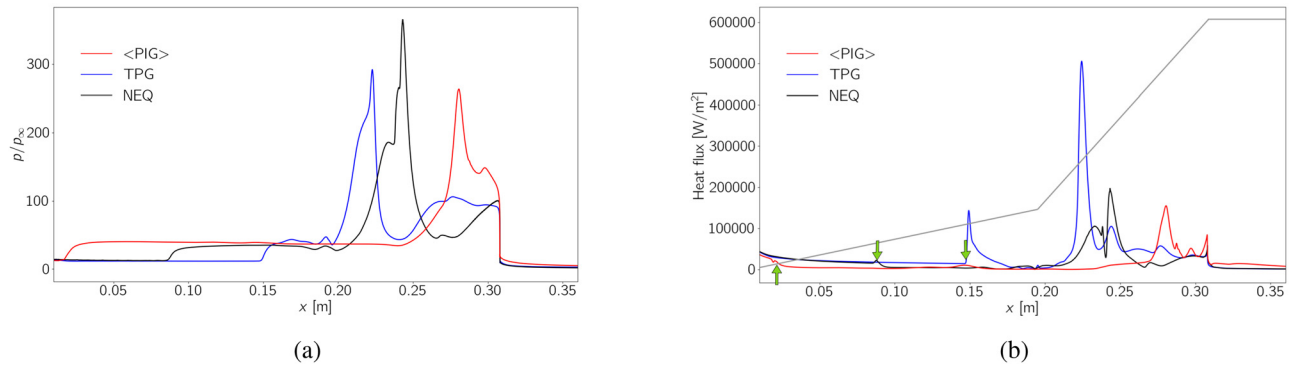
FIG. 19. Comparison of surface aerothermal loads of (a) normalized pressure and (b) heat flux, for the 15°–55° double-wedge: perfect ideal gas (time averaged), thermally perfect gas, and nonequilibrium gas model.

Figure 19 shows a comparison of the surface quantities between the three models, where for the unsteady case a time-averaged distribution over the periodic cycle is plotted. The TPG and NEQ models result in a qualitatively similar normalized pressure distribution. The first increase in pressure corresponding to the detachment of the boundary layer takes place in different locations for the three models, occurring at $x = 0.021$ m when vibrational excitation is not accounted for, at $x = 0.088$ m when the nonequilibrium relaxation time is accounted for and more downstream, at $x = 0.148$ m when equilibrium is enforced. The pressure plateau downstream of the separation point is similar for all three models, which shows that the effects of vibrational excitation in surface pressure are minimal in this region. For the models that account for molecular vibration, the second increase in pressure results from reattachment of the boundary layer, which occurs more gradually for the NEQ model. The more abrupt reattachment in the TPG solution leads to a larger pressure gradient in this region, and just downstream to a 9% larger spike resulting from shock impingement. The time-averaged surface pressure obtained with the PIG model results in a pressure peak resulting from shock impingement that is of similar intensity as the one obtained with a NEQ model. As for the surface heating distributions, all three models result in qualitatively different curves. While for the TPG model, a heat flux spike is generated in the region of boundary layer detachment on the surface of the fore wedge, this transition is smooth in the NEQ solution. In contrast, the transition between boundary layer reattachment and shock impingement is smoother for the TPG model, which results in a single large peak of heat flux of about 500 000 W/m² in this region. The NEQ solution, on the other hand, exhibits two smaller heat flux peaks that are separated by a sudden drop of this quantity, which is a consequence of the SBLI separated region between reattachment and shock impingement. The PIG model results in a long region of low heat flux corresponding to the very large separation bubble. Several spikes are obtained in the surface time-averaged heat flux near the expansion corner, where most of the interaction features take place. It is worth noticing that, even though the averaged heat flux is overall much lower for this model than for the other two, from a design perspective it is essential to consider the instantaneous spike at $t_0 + 0.002$ s that results in the highest value of heat flux observed in the numerical results.

VII. CONCLUSIONS

In the present study, CFD computations are carried out to investigate viscous laminar shock interference in CO_2-dominated flows in thermal nonequilibrium. For this purpose, a Mach 9 hypersonic flow is simulated over different double-wedge configurations by increasing the aft wedge angle. A two-temperature model is used to account for vibrational relaxation. Numerical results show that, as the aft wedge angle is increased, the separated region generated by the compression corner continuously thickens and the separation point moves toward the leading edge. Except for the lower angle, a local type VI pattern occurs as a result of the interaction between the leading shock and the detachment shock generated by the recirculation bubble. The complexity of the overall mechanism of interaction is also increased as the geometry changes in the following manner:

- The 15°–40° geometry results in a type VI interaction pattern, resulting from the interference of the leading, detachment, and reattachment shocks.
- The 15°–45° geometry results in a local type VI interaction near the compression corner and another type VI pattern as the main mechanism of interaction.
- The 15°–50° geometry results in a type VI pattern near the compression corner and a type V pattern as the main mechanism of interaction, resulting in relatively weak shock impingement with no boundary layer separation.
- The 15°–55° geometry results in a flow pattern similar to the previous one, but in this case shock impingement causes a second region of boundary layer separation (besides the one in the compression corner) accompanied by additional detachment and reattachment shocks.

When it comes to the distribution of surface loads, except for the higher angle, the maximum values of heat flux and surface pressure result from reattachment of the boundary layer downstream of the compression corner. For the 15°–55° double-wedge, the most severe surface loads are a consequence of shock impingement on the wall, with a peak of pressure and heat flux 2.2 and 2.5 times larger than for the 15°–50° geometry, respectively.

To better understand the role of vibrational relaxation in the mechanisms of interaction, additional simulations are performed with more simplified models: a perfect ideal gas model that does not

account for rotational/vibrational/electronic excitation of molecules and a thermally perfect gas model that implicitly considers vibrational excitation but enforces thermal equilibrium. The study shows that the more energy is transferred to the vibrational degrees of freedom, the lower post-shock temperatures are obtained. This tends to reduce the post-shock density, leading to weaker shock interactions characterized by delayed onsets of separation and reduced separation regions, lower shock angles, and smaller standoff distances. Regarding the models considered in this study, this means that the perfect ideal gas model, which considers no vibration at all, results in the stronger interactions and more complex patterns with a higher number of flow features, followed by the thermal nonequilibrium flow physics that accounts for the relaxation time necessary for the energy absorption process to occur, and finally the thermally perfect gas model, which enforces instantaneous energy transfer between the internal energy modes. The thermally perfect gas model tends to yield a thinner boundary layer upon reattachment, which results in the most severe surface loads of heat flux and pressure. While the different models have a large impact on the flow features as well as distributions of surface quantities, i.e., location and intensity of pressure and heat flux peaks, the surface plateau pressure and heating in the post-leading shock and separation regions are not significantly affected. This is likely due to the relatively low temperatures obtained in these regions and minimal activation of the vibrational modes. Moreover, the study shows that accounting for real gas effects stabilizes the flow in the case of the highest angle, for which an unsteady strong coupling between the separated region and the entire shock system is obtained for the perfect ideal gas model. It is observed that vibrational excitation delays the threshold of unsteadiness, even more for the case of the thermally perfect gas model that considers thermal equilibrium.

It is overall concluded that vibrational relaxation plays an active role in the mechanisms of shock interference for CO_2 mixtures, since the assumptions of different simplified models result in significant differences in terms of qualitative flow patterns as well as distributions of surface aerothermal loads. Still in regard to the scope of a continuum-based macroscopic approach, future work could consider more detailed thermochemical models in view of achieving convergence of the flow physics.

AUTHOR DECLARATIONS
Conflict of Interest

No conflicts of interest to disclose.

DATA AVAILABILITY

The data that support the findings of this study are available from the corresponding author upon request.

REFERENCES

[1] J. D. Watts, "Flight experience with shock impingment and interference heating on the X-15-a research airplane," Technical Paper No. TM X-1669, NASA, 1968.

[2] B. Edney, "Anomalous heat transfer and pressure distributions on blunt bodies at hypersonic speeds in the presence of an impinging shock," Technical Report No. FFA-115, The Aeronautical Research Institute of Sweden, 1968.

[3] A. Durna and B. Celik, "Time-periodic shock interaction mechanisms over double wedges at Mach 7," Shock Waves **29**, 381 (2019).

[4] A. S. Durna and B. Celik, "Effects of double-wedge aft angle on hypersonic laminar flows," AIAA J. **58**, 1689–1703 (2020).

[5] J. Olejniczak, M. Wright, and G. Candler, "Numerical study of inviscid shock interactions on double-wedge geometries," J. Fluid Mech. **352**, 1–25 (1997).

[6] O. Tumuklu, D. A. Levin, and J. M. Austin, "Shock-shock interactions for a double wedge configuration in different gases," AIAA Paper No. 2015-1520, 2015.

[7] O. Tumuklu, D. A. Levin, S. F. Gimelshein, and J. M. Austin, "Factors influencing flow steadiness in laminar boundary layer shock interactions," AIP Conf. Proc. **1786**, 050005 (2016).

[8] M. R. Youssefi and D. Knight, "Assessment of CFD capability for hypersonic shock wave laminar boundary layer interactions," Aerospace **4**, 25 (2017).

[9] J. Hao and C.-Y. Wen, "Effects of vibrational nonequilibrium on hypersonic shock-wave/laminar boundary-layer interactions," Int. Commun. Heat Mass Transfer **97**, 136–142 (2018).

[10] A. Khraibut and S. Gai, "Flow steadiness over a double wedge at Mach 7 including effect of trailing edge expansion," AIAA Paper No. 2018-5388, 2018.

[11] A. S. Durna, M. El Hajj Ali Barada, and B. Celik, "Shock interaction mechanisms on a double wedge at Mach 7," Phys. Fluids **28**, 096101 (2016).

[12] G. Kumar and A. De, "Role of corner flow separation in unsteady dynamics of hypersonic flow over a double wedge geometry," Phys. Fluids **33**, 036109 (2021).

[13] D. Vatansever and B. Celik, "Unsteady shock interaction mechanisms of high enthalpy reacting flows over double wedges at Mach 7," Phys. Fluids **33**, 056110 (2021).

[14] G. Candler, "Computation of thermo-chemical nonequilibrium Martian atmospheric entry flows," in *Proceedings of 5th Joint Thermophysics and Heat Transfer Conference* (American Research Central, 1990).

[15] C. Park, J. T. Howe, R. L. Jaffe, and G. V. Candler, "Review of chemical-kinetic problems of future NASA missions, II: Mars entries," J. Thermophys. Heat Transfer **8**, 9–23 (1994).

[16] C. Windisch, B. U. Reinartz, and S. Müller, "Investigation of unsteady Edney type IV and VII shock-shock interactions," AIAA J. **54**, 1846–1861 (2016).

[17] I. Armenise and E. Kustova, "On different contributions to the heat flux and diffusion in non-equilibrium flows," Chem. Phys. **428**, 90–104 (2014).

[18] E. Kustova and E. Nagnibeda, "On a correct description of a multi-temperature dissociating Co_2 flow," Chem. Phys. **321**, 293–310 (2006).

[19] E. V. Kustova, E. A. Nagnibeda, Y. D. Shevelev, and N. G. Syzranova, "Non–equilibrium supersonic CO_2 flows with real gas effects near a blunt body," AIP Conf. Proc. **1084**, 831–836 (2008).

[20] E. Kustova, E. Nagnibeda, Y. Shevelev, and N. Syzranova, "Comparison of different models for non-equilibrium Co_2 flows in a shock layer near a blunt body," Shock Waves **21**, 273–287 (2011).

[21] C. Garbacz, W. Maier, J. Scoggins, T. Economon, T. Magin, J. Alonso, and M. Fossati, "Shock interactions in inviscid air and CO_2-N_2 flows in thermochemical non-equilibrium," Shock Waves **31**, 239–253 (2021).

[22] A. Swantek, "The role of aerothermochemistry in double cone and double wedge flows," Ph.D. thesis (University of Illinois, 2012).

[23] T. Hashimoto, "Experimental investigation of hypersonic flow induced separation over double wedges," J. Therm. Sci. **18**, 220–225 (2009).

[24] D. A. Stewart and Y. K. Chen, "Hypersonic convective heat transfer over 140-deg blunt cones in different gases," J. Spacecr. Rockets **31**, 735–743 (1994).

[25] B. R. Hollis and J. N. Perkins, "High-enthalpy and perfect-gas heating measurements on a blunt cone," J. Spacecr. Rockets **33**, 628–634 (1996).

[26]M. Netterfield, F. Mazoue, L. Marraffa, D. Kastell, and G. Eitelberg, "Experiments and computations on a blunt body in a high enthalpy CO_2 flow," AIAA Paper No. 96-1804, 1996.

[27]C. Wen, "Hypervelocity flow over spheres," Ph.D. thesis (California Institute of Technology, 1996).

[28]M. Sharma, A. Swantek, W. Flaherty, J. Austin, S. Doraiswamy, and G. Candler, "Evaluation of hypervelocity carbon dioxide blunt body experiments in an expansion tube facility," AIAA Paper No. 2011-136, 2011.

[29]S. Gu, "Mars entry afterbody radiative heating: An experimental study of nonequilibrium CO_2 expanding flow," Ph.D. thesis (The University of Queensland, 2017).

[30]D. Liao, S. Liu, J. Huang, H. Jian, A. Xie, and Z. Wang, "Measurement and numerical simulation of shock standoff distances over hypersonic spheres in CO_2 in a ballistic range," Shock Waves **30**, 131–138 (2020).

[31]T. D. Economon, F. Palacios, S. R. Copeland, T. W. Lukaczyk, and J. J. Alonso, "SU2: An open-source suite for multiphysics simulation and design," AIAA J. **54**, 828–846 (2016).

[32]J. B. Scoggins, V. Leroy, G. Bellas-Chatzigeorgis, B. Dias, and T. E. Magin, "Mutation^{++}: MUlticomponent Thermodynamic And Transport properties for IONized gases in C++," SoftwareX **12**, 100575 (2020).

[33]P. Gnoffo, R. Gupta, and J. Shinn, "Conservation equations and physical models for hypersonic air flows in thermal and chemical nonequilibrium," NASA Technical Paper No. 2867, 1989, p. 158.

[34]C. Park, "Review of chemical-kinetic problems of future NASA missions. I - Earth entries," J. Thermophys. Heat Transfer **7**, 385–398 (1993).

[35]I. Armenise, P. Reynier, and E. Kustova, "Advanced models for vibrational and chemical kinetics applied to Mars entry aerothermodynamics," J. Thermophys. Heat Transfer **30**, 705–720 (2016).

[36]M. Camac, "CO_2 relaxation processes in shock waves," in *Fundamental Phenomena in Hypersonic Flow* (Cornell U.P., Ithaca, NY, 1966), pp. 195–215.

[37]C. Park, "Assessment of two-temperature kinetic model for ionizing air," J. Thermophys. Heat Transfer **3**, 233–244 (1989).

[38]L. Landau and E. Teller, Phys. Z. Sowjetunion **10**, 34–38 (1936).

[39]R. C. Millikan and D. R. White, "Systematics of vibrational relaxation," J. Chem. Phys. **39**, 3209–3213 (1963).

[40]C. R. Wilke, "A viscosity equation for gas mixtures," J. Chem. Phys. **18**, 517–519 (1950).

[41]A. Eucken, "Über das wärmeleitvermögen, die spezifische wärme und die innere reibung der gase," Phys. Z. **14**, 324–332 (1913).

[42]F. Palacios, S. Copeland, A. Lonkar, and J. Alonso, "Adjoint-based goal-oriented mesh adaptation for nonequilibrium hypersonic flows," AIAA Paper No. 2013-0552, 2013.

[43]W. T. Maier, J. T. Needels, C. Garbacz, F. Morgado, J. J. Alonso, and M. Fossati, "SU2-NEMO: An open-source framework for high-Mach nonequilibrium multi-species flows," Aerospace **8**, 193 (2021).

[44]C. Garbacz, M. Fossati, W. Maier, J. J. Alonso, J. Scoggins, T. Magin, and T. D. Economon, "Numerical study of shock interference patterns for gas flows with thermal nonequilibrium and finite-rate chemistry," AIAA Paper No. 2020-1805, 2020.

[45]M.-S. Liou and C. J. Steffen, "A new flux splitting scheme," J. Comput. Phys. **107**, 23–39 (1993).

[46]A. Loseille and R. Loehner, "Boundary layer mesh generation and adaptivity," AIAA Paper No. 2011-894, 2011.

[47]A. Loseille and V. Menier, "Serial and parallel mesh modification through a unique cavity-based primitive," in *Proceedings of the 22nd International Meshing Roundtable*, edited by J. Sarrate and M. Staten (Springer International Publishing, Cham, 2014), pp. 541–558.

[48]A. Loseille, V. Menier, and F. Alauzet, "Parallel generation of large-size adapted meshes," Procedia Eng. **124**, 57–69 (2015).

[49]A. Loseille, "Unstructured mesh generation and adaptation," in *Handbook of Numerical Methods for Hyperbolic Problems - Applied and Modern Issues*, edited by R. Abgrall and C.-W. Shu (Elsevier, 2017), pp. 263–302.

[50]C. L. Running, T. J. Juliano, J. S. Jewell, M. P. Borg, and R. L. Kimmel, "Hypersonic shock-wave/boundary-layer interactions on a cone/flare," Exp. Therm. Fluid Sci. **109**, 109911 (2019).

[51]F. G. Blottner, M. Johnson, and M. Ellis, "Chemically reacting viscous flow program for multi-component gas mixtures," Technical Report No. SC-RR-70-754, Sandia Labs., Albuquerque, NM, 1971.